

Modelling large mass removal in adsorption columns

T. G. Myers

Centre de Recerca Matemàtica, Edifici C, Campus Bellaterra, 08193 Bellaterra, Spain

M. Calvo-Schwarzwalder

Centre de Recerca Matemàtica, Edifici C, Campus Bellaterra, 08193 Bellaterra, Spain

F. Font¹

Department of Fluid Mechanics, Universitat Politècnica de Catalunya, 08019 Barcelona, Spain

A. Valverde

Department of Chemical Engineering, Universitat Politècnica de Catalunya, 08028 Barcelona, Spain.

Abstract

A mathematical model is developed to describe column adsorption when the contaminant constitutes a significant amount of the fluid. This requires modelling the variation of pressure and velocity, in addition to the usual advection-diffusion-adsorption and kinetic equations describing concentration and adsorption rates. The model builds on previous work based on a linear kinetic equation, to include both physical and chemical adsorption. A semi-analytical solution is developed and validated against a numerical solution. The model is tested against experimental data for the adsorption of large quantities of CO₂ from a helium mixture, with a CO₂ volume fraction ranging from 14% to 69%, and a N₂ mixture with 16% to 33% CO₂ volume fraction. Our results show a significant improvement with respect to models for the removal of trace amounts of contaminant.

Keywords: Contaminant removal, Pollutant removal, Adsorption, Fluid dynamics, Mathematical model
2010 MSC: 35Q35

1. Introduction

Column sorption is a practical method for removing a contaminant from a carrier fluid. It has uses in environmental applications such as greenhouse gas capture, groundwater remediation and biogas cleansing as well as industrial uses such as the purification of biopharmaceutical products, the cleansing of flue gases, biofuel purification and many more. Given the importance of the process, particularly in environmental remediation, researchers constantly strive to improve and optimise the technology.

A key element in the optimisation process is the development and understanding of models for adsorption. In general mathematical models have focussed on the removal of trace amounts

¹Corresponding author: francesc.font@upc.edu

of contaminants subject to a physisorption process. The base model for this situation results in a system of two equations, describing the evolution of the cross-sectionally averaged contaminant concentration and amount adsorbed through a column. Perhaps the most well-known solution to the system is that of Bohart and Adams [1] which predicts the concentration throughout the column and provides a simple expression for the breakthrough curve (the outlet concentration). Their model is frequently referred to as the Thomas model, with a minor rearrangement it is also referred to as the Bed Depth Service Time Model. The Bohart-Adams model is based on an adsorption rate similar to the standard Langmuir model but with zero desorption. Although it can match certain data sets with others it shows very poor agreement. Amundsen [2] attempted to improve agreement by shifting the time axis slightly (by the column length divided by the interstitial fluid velocity). In practice this makes a negligible difference. The Yoon-Nelson model [3] takes the same mathematical form as Bohart-Adams but is based on the probability of a molecule escaping the column outlet. In addition to these theoretically based models there exist many empirical ones. Shafeeyan *et al* [4] review over “three decades” of modelling: all models follow the same format and are solved numerically. They go on to state that since the computational time is so large it would be desirable to develop reduced models with good prediction capabilities and so facilitate optimisation. Li *et al* [5] state that "modelling methods with mathematical equations are still rare in the existing publications". A discussion of errors and inaccuracies of breakthrough models is provided in [6].

When dealing with the removal of a significant quantity of material a model should account for the effect of the mass loss, for example on velocity and pressure. However, it is common practice to employ the Bohart-Adams form to fit breakthrough curves with a 15% v/v or higher content of contaminant [7–9], or determine numerical solutions of single-component constant velocity models [10–12]. Certain studies differentiate between the fluid components but still impose constant velocity [13]. In studies where the effect of the removal of large quantities of contaminant is accounted for (20% up to 75% v/v, for instance) [14–16], a numerical solution is applied using the Ergun equation [17] to relate the velocity with the pressure drop, without considering the sink term in the conservation of momentum. Dantas *et al* [18, 19] employ the Ergun equation, a pseudo-first order kinetic equation (also known as the linear driving force model) and include temperature effects. Their system requires a full numerical solution.

In a series of papers our group has explained why the Bohart-Adams and related models may be inaccurate [6, 20, 21] and then produced accurate models to describe chemisorption [22], intra-particle diffusion [23, 24] and extraction [25]. However, all of these models are designed to deal with the removal of trace amounts of contaminants and so are not suitable to deal with large emissions, such as flue or exhaust gases.

In [26] a model was developed and analysed to describe the capture of significant quantities of CO₂, where the adsorption was also described by the linear driving force model. Although mathematically convenient, this form presents physical issues in that adsorption occurs independently of whether there is a contaminant in the fluid or not. It also neglects desorption. Valverde *et al* [23] demonstrated that this type of kinetic equation can predict negative concentrations near the contaminant front.

In the present work we will extend the large mass removal model of [26], applying a physically realistic kinetic equation which encompasses both physical and chemical adsorption. In §2 we discuss the experimental setup and derive the general mathematical model. After introducing appropriate non-dimensional variables in §3 it is demonstrated that the model may be simplified without losing accuracy. In §4 we present analytical solutions to the reduced

model and verify them by comparison with a numerical solution. Results of the model are then presented, demonstrating the effect of key parameters, such as contaminant volume fraction, system temperature, or flow rate. In §5 we discuss practical applications of the model and compare the analytical solutions against experimental data for the removal of CO_2 from a CO_2/N_2 mixture. We also discuss an alternative way to present the data which makes the correct model easier to identify.

2. Mathematical Model

In this section we first present the experimental set up that motivates the mathematical model and then discuss the model in the context of removal of large amounts of contaminant.

2.1. Description of the experimental set up and key variables

As depicted in Fig. 1, we consider a column of length L and radius R filled with a porous material, the adsorbent, that occupies a fraction $1 - \epsilon$ of the total space available. At the inlet, we introduce a fluid mixture with fixed contaminant and carrier gas volume fractions ϕ_1 and ϕ_2 (with $\phi_1 + \phi_2 = 1$) at a constant velocity u_0 . The contaminant attaches to the adsorbent's surface as the mixture flows through the column. The concentration of contaminant is measured at the outlet to record the *breakthrough curve*. To model this process, at a minimum, we must calculate the concentration of both carrier fluid and contaminant, the amount adsorbed, pressure and velocity fields. In Myers *et al.* [20] temperature variation was also included in the initial system, but later shown to be negligible. This is consistent with the numerical work of Li *et al* [5] on the removal of CO_2 , which exhibits a temperature rise of at most a few degrees, consequently we restrict the present analysis to the isothermal case.

In keeping with standard practice we will work with cross-sectionally averaged quantities. Careful derivations of related averaged equations and their accuracy may be found in [21, 22, 27].

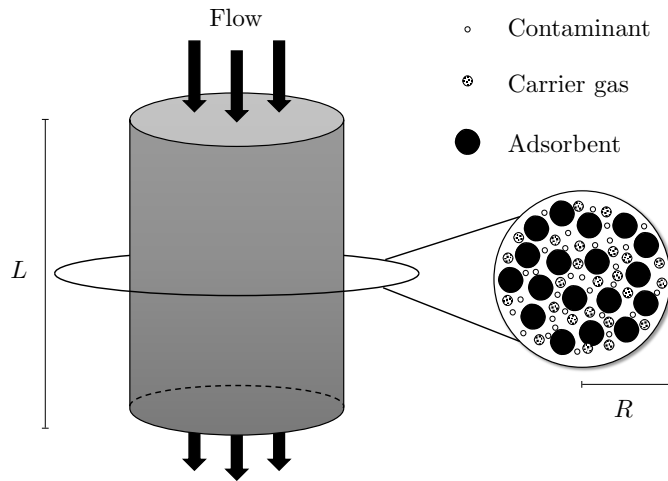


Figure 1: Schematic of the experimental setup. We consider a column of length L and radius R that is packed with a porous, adsorbent material. A gas mixture consisting of a carrier gas and a contaminant is forced into the column at the inlet and the concentrations at the outlet are measured throughout the experiment.

2.2. Governing equations

Let c_1, c_2 be the concentration of contaminant and carrier gas. In the present analysis we work with mol/m³, but kg/m³ is also common in column adsorption studies, the conversion is trivial. Following [26], the system of equations is

$$\frac{\partial c_1}{\partial t} + \frac{\partial}{\partial x}(uc_1) = D \frac{\partial^2 c_1}{\partial x^2} - \frac{1-\epsilon}{\epsilon} \rho_a \frac{\partial q}{\partial t}, \quad (1a)$$

$$\frac{\partial c_2}{\partial t} + \frac{\partial}{\partial x}(uc_2) = D \frac{\partial^2 c_2}{\partial x^2}. \quad (1b)$$

$$p = R_g T (c_1 + c_2), \quad (1c)$$

$$-\frac{\partial p}{\partial x} = \alpha (M_1 c_1 + M_2 c_2) u^2 + \left(\beta + \frac{(1-\epsilon)}{\epsilon} \rho_a M_1 \frac{\partial q}{\partial t} \right) u, \quad (1d)$$

$$\frac{\partial q}{\partial t} = \dot{Q}, \quad (1e)$$

where D is the diffusion coefficient, ρ_a is the particle apparent density, $R_g = 8.31$ J/K·mol is the universal gas constant, T is the temperature, M_1, M_2 are the molar masses of the contaminant and the carrier gas respectively. The void fraction ϵ is assumed constant throughout the column. The constants α and β stem from the Ergun relation [26], and are defined by

$$\alpha = \frac{1.75(1-\epsilon)}{d_p \epsilon}, \quad \beta = \frac{150 \mu_g (1-\epsilon)^2}{d_p^2 \epsilon^2}, \quad (2)$$

where d_p is the diameter of the adsorbing particles and μ_g is the gas viscosity.

Note, the original paper by Myers *et al.* [26] used slightly different notation and fitted for the unknown adsorbed material density. Here we will fit to the more standard adsorption coefficient.

2.3. Boundary and initial conditions

The inlet condition is not trivial: we assume that the pressure at the inlet is higher than the pressure at the outlet, i.e.,

$$p_{in} = p_a + \Delta p, \quad (3)$$

where p_a is the ambient (outlet) pressure and Δp is the pressure drop, which must be a function of time to ensure that the gas velocity at the inlet remains constant. Using the ideal gas law, for a given volume fraction ϕ_i , the concentration of species i just upstream of the inlet is

$$c_i(0^-, t) = \frac{\phi_i p_{in}(t)}{R_g T} = \frac{\phi_i}{R_g T} (p_a + \Delta p) = \frac{\phi_i p_a}{R_g T} \left(1 + \frac{\Delta p}{p_a} \right) = c_{i0} \left(1 + \frac{\Delta p}{p_a} \right), \quad (4)$$

where T is the temperature and R_g the universal gas constant. If the pressure drop is small ($\Delta p \ll p_a$) then the inlet concentrations may be considered approximately constant, i.e., $c_i(0^-, t) \approx c_{i0}$. We will restrict ourselves to this case since most practical applications have very low velocities and therefore very small pressure drops along the column.

The initial and boundary conditions are then:

$$u_0 c_i(0^-, t) = \left(u c_i - D \frac{\partial c_i}{\partial x} \right) \Big|_{x=0^+}, \quad \frac{\partial c_i}{\partial x} \Big|_{x=L} = 0, \quad (5)$$

$$p(0, t) = p_a + \Delta p, \quad p(L, t) = p_a, \quad (6)$$

with $i = 1, 2$.

Initially, there is neither free nor adsorbed contaminant in the column, hence

$$c_1(x, 0) = q(x, 0) = 0. \quad (7a)$$

The available space in the column is initially occupied by the carrier gas. From Eq. (1c) we find

$$c_2(x, 0) = \frac{p(x, 0)}{R_g T}, \quad (7b)$$

while for the pressure we impose an initially linear profile

$$p(x, 0) = p_a + \left(1 - \frac{x}{L}\right) \Delta p(0). \quad (7c)$$

2.4. Choice of kinetic equation

The function \dot{Q} is key to correctly capturing the adsorption behaviour. Following the work of [5, 18, 19] in [26], the authors use the linear driving force model

$$\dot{Q}(q) = k_L(q_e - q), \quad (8)$$

where k_L is the adsorption rate for this particular model. As previously mentioned, this simple model has physical issues. For instance adsorption occurs whenever $q < q_e$, regardless of whether contaminant is present or not.

Here we employ a more general form, which may describe both chemical and physical adsorption, namely the Sips equation [28]

$$\dot{Q}(q, c_1) = k_a c_1^m (q_{max} - q)^n - k_d q^n, \quad (9)$$

where k_a and k_d are the adsorption and desorption rates respectively and we assume only component 1 is adsorbed. The maximum amount that may be adsorbed is denoted q_{max} , in general this is greater than the amount actually adsorbed. The powers m and n are related to the partial orders of reaction of the contaminant and the available adsorption sites in the global reaction



with \mathbb{C} and \mathbb{A} referring to the free contaminant and adsorbent molecules and \mathbb{AC} to the reaction output. We will assume m, n to be integers but note that with a chain of reactions it is possible that they take non-integer values. The well-known Langmuir sink, describing physisorption, may be retrieved in the case $(m, n) = (1, 1)$.

When adsorption balances desorption, $\dot{Q} = 0$, the isotherm is obtained. Denoting the equilibrium adsorbed amount q_e for a given inlet contaminant concentration c_{10} , equation (9) may be rearranged to define the Sips isotherm

$$q_e = \frac{q_{max} K^{1/n} c_{10}^{m/n}}{1 + K^{1/n} c_{10}^{m/n}}, \quad (11)$$

where $K = k_a/k_d$ is the equilibrium constant, whose units ($\text{m}^{3m}\text{kg}^{n-1}\text{mol}^{1-m-n}$) depend on the value of m and n . The values of q_{max} and K may be determined experimentally from the recorded isotherms, as will be shown in §5.

3. Model Simplification

At present the model consists of Eqs. (1), with \dot{Q} defined in Eq. (9). The boundary and initial conditions are defined in Eqs. (5–7). In this state it is difficult to make any analytical progress, consequently we now examine the relative size of terms by non-dimensionalising the system.

3.1. Non-dimensional formulation

We introduce the scaled variables

$$\hat{c}_1 = \frac{c_1}{c_{10}}, \quad \hat{c}_2 = \frac{c_2}{c_{20}}, \quad \hat{q} = \frac{q}{q_{max}}, \quad \hat{u} = \frac{u}{\mathcal{U}}, \quad \hat{x} = \frac{x}{\mathcal{L}}, \quad \hat{p} = \frac{p - p_a}{\mathcal{P}}, \quad \hat{t} = \frac{t}{\mathcal{T}}, \quad (12)$$

where the scales \mathcal{U} , \mathcal{L} , \mathcal{P} and \mathcal{T} are yet to be determined. The velocity scale is chosen as the constant inlet value $\mathcal{U} = u_0$. Since the focus is on the adsorption process, we choose $\mathcal{T} = 1/(k_a c_{10}^m q_{max}^{n-1})$ to balance the time derivative and adsorption terms in Eq. (9). The length scale is determined by balancing the advection and sink terms in Eq. (1a), $\mathcal{L} = \epsilon \mathcal{U} \mathcal{T} c_{10} / [(1 - \epsilon) \rho_a q_{max}]$. The pressure scale can be determined through Eq. (1d). Upon replacing the dimensional quantities by their scaled counterparts, the Ergun equation (1d) becomes

$$-\mathcal{P} \frac{\partial \hat{p}}{\partial \hat{x}} = \alpha \mathcal{L} \mathcal{U}^2 (M_1 c_{10} \hat{c}_1 + M_2 c_{20} \hat{c}_2) \hat{u}^2 + \beta \mathcal{L} \mathcal{U} \hat{u} + \frac{(1 - \epsilon) \rho_a M_1 q_{max} \mathcal{L} \mathcal{U}}{\epsilon \mathcal{T}} \hat{u} \frac{\partial \hat{q}}{\partial \hat{t}}. \quad (13)$$

Assuming approximately Darcy flow, we choose $\mathcal{P} = \beta \mathcal{L} \mathcal{U}$ to balance the pressure gradient and the second term on the right-hand side.

The final set of non-dimensional equations is now

$$\delta_1 \frac{\partial \hat{c}_1}{\partial \hat{t}} + \frac{\partial}{\partial \hat{x}} (\hat{u} \hat{c}_1) = \delta_2 \frac{\partial^2 \hat{c}_1}{\partial \hat{x}^2} - \frac{\partial \hat{q}}{\partial \hat{t}}, \quad (14a)$$

$$\delta_1 \frac{\partial \hat{c}_2}{\partial \hat{t}} + \frac{\partial}{\partial \hat{x}} (\hat{u} \hat{c}_2) = \delta_2 \frac{\partial^2 \hat{c}_2}{\partial \hat{x}^2}, \quad (14b)$$

$$1 + \delta_3 \hat{p} = \phi_1 \hat{c}_1 + \phi_2 \hat{c}_2, \quad (14c)$$

$$-\frac{\partial \hat{p}}{\partial \hat{x}} = \delta_4 (\delta_5 \hat{c}_1 + \hat{c}_2) \hat{u}^2 + \left(1 + \delta_6 \frac{\partial \hat{q}}{\partial \hat{t}}\right) \hat{u}, \quad (14d)$$

$$\frac{\partial \hat{q}}{\partial \hat{t}} = \hat{c}_1^m (1 - \hat{q})^n - \delta_7 \hat{q}^n. \quad (14e)$$

These are subject to the boundary and initial conditions

$$1 + \delta_3 \hat{p} = \left(\hat{u} \hat{c}_1 - \delta_2 \frac{\partial \hat{c}_1}{\partial \hat{x}} \right) \Big|_{\hat{x}=0}, \quad \frac{\partial \hat{c}_1}{\partial \hat{x}} \Big|_{\hat{x}=\hat{L}} = 0, \quad \hat{c}_1(\hat{x}, 0) = 0, \quad (15a)$$

$$1 + \delta_3 \hat{p} = \left(\hat{u} \hat{c}_2 - \delta_2 \frac{\partial \hat{c}_2}{\partial \hat{x}} \right) \Big|_{\hat{x}=0}, \quad \frac{\partial \hat{c}_2}{\partial \hat{x}} \Big|_{\hat{x}=\hat{L}} = 0, \quad \phi_2 \hat{c}_2(\hat{x}, 0) = 1 + \delta_3 \hat{p}_{in}(\hat{x}), \quad (15b)$$

$$\hat{p}(\hat{L}, \hat{t}) = 0, \quad \hat{p}(\hat{x}, 0) = \hat{p}_{in}(\hat{x}) = \Delta \hat{p}(0) \left(1 - \frac{\hat{x}}{\hat{L}}\right), \quad (15c)$$

$$\hat{q}(\hat{x}, 0) = 0, \quad (15d)$$

with $\Delta\hat{p}(0) = \Delta p(0)/\mathcal{P}$. Evaluating (14d) at $t = 0$ and combining it with (15c), gives

$$\delta_4 \hat{c}_2(\hat{x}, 0) \hat{u}(\hat{x}, 0)^2 + \hat{u}(\hat{x}, 0) - \frac{\Delta\hat{p}(0)}{\hat{L}} = 0. \quad (16)$$

The positive roots of the polynomial (16) provide an initial profile for \hat{u} .

Besides the volume fractions ϕ_1 and ϕ_2 , the non-dimensional model has 7 additional dimensionless quantities, defined by

$$\begin{aligned} \delta_1 &= \frac{\mathcal{L}}{\mathcal{U}\mathcal{T}}, & \delta_2 &= \frac{D}{\mathcal{L}\mathcal{U}} & \delta_3 &= \frac{\mathcal{P}}{p_a}, & \delta_4 &= \frac{\alpha M_2 c_{20} \mathcal{U}^2 \mathcal{L}}{\mathcal{P}}, \\ \delta_5 &= \frac{c_{10} M_1}{c_{20} M_2}, & \delta_6 &= \frac{(1-\epsilon)\rho_a M_1 q_{max} \mathcal{L}\mathcal{U}}{\epsilon \mathcal{T} \mathcal{P}}, & \delta_7 &= \frac{k_d}{k_a c_{10}^m} = \frac{1}{K c_{10}^m}. \end{aligned} \quad (17)$$

The value of k_a is not easily directly determined by experiments, hence we consider it a free parameter in the current model. Replacing the scales we obtain

$$\begin{aligned} \delta_1 &= \frac{\epsilon c_{10}}{(1-\epsilon)\rho_a q_{max}}, & \delta_2 &= \left(\frac{(1-\epsilon)\rho_a D c_{10}^{m-1} q_{max}^n}{\epsilon u_0^2} \right) k_a \\ \delta_3 &= \left(\frac{\epsilon \beta u_0^2}{(1-\epsilon)\rho_a p_a c_{10}^{m-1} q_{max}^n} \right) \frac{1}{k_a}, \\ \delta_4 &= \frac{\alpha M_2 c_{20} u_0}{\beta}, & \delta_6 &= \left(\frac{(1-\epsilon)\rho_a M_1 c_{10}^m q_{max}^n}{\epsilon \beta} \right) k_a. \end{aligned} \quad (18)$$

The non-dimensional equilibrium value $\hat{q}_e = q_e/q_{max}$ is

$$\hat{q}_e = \frac{1}{1 + \delta_7^{1/n}}. \quad (19)$$

3.2. Interpretation of parameters

Since \mathcal{L} and \mathcal{T} are both chosen to balance the adsorption terms, the ratio \mathcal{L}/\mathcal{T} may be interpreted as an adsorption velocity. Therefore, the parameter $\delta_1 = \mathcal{L}/(\mathcal{T}u_0)$ is the ratio of the adsorption velocity to the fluid velocity and hence represents a form of Damköhler number. The non-dimensional parameter $\delta_2 = D/(\mathcal{L}u_0)$ represents the ratio of the diffusive transport rate D/\mathcal{L} to the advective transport rate u_0 and is therefore an inverse Péclet number. The third parameter $\delta_3 = \mathcal{P}/p_a$ is the Darcy pressure scale relative to the ambient pressure. In §5 we demonstrate that for the cases studied, which are representative of adsorption from a gas stream, $\delta_1 = \mathcal{O}(10^{-3})$, $\delta_2 = \mathcal{O}(10^{-1})$ or smaller and δ_3 is $\mathcal{O}(10^{-2})$ or smaller.

The parameter δ_4 relates the kinetic energy of the carrier fluid to the pressure gradient driving the flow or viscous resistance (equivalent since the two are balanced). Then δ_6 relates the energy loss due to mass removal to the viscous resistance. Since the flow is driven by the pressure gradient we expect $\delta_4, \delta_6 \ll 1$. In §5 they are shown to be $\mathcal{O}(10^{-3})$.

The parameter δ_5 represents the ratio of densities and will vary depending on the contaminant, carrier fluid and volume fractions. We may assume this quantity to be $\mathcal{O}(1)$.

Finally, $\delta_7 = k_d/(k_a c_{10}^m)$ represents the ratio of the adsorption to the desorption time scales. If the value of δ_7 is small, it suggests that adsorption dominates. Although our focus is on adsorption processes we will retain it in the reduced system of equations to permit modelling of filters where both processes are comparable or to include regeneration of filters. If its value is significantly very small then we lose nothing through its retention. It is also important to retain δ_7 to correctly model the isotherm and determine the value k_d/k_a .

4. Solution methods

In this section we first take advantage of the anticipated small size of certain terms to reduce the problem to a more tractable set of equations (the size of neglected terms is verified in §4.4). By applying a travelling wave substitution we are then able to obtain exact solutions for the cases where $m = 1$ and $n = 1, 2$. Further solutions may be possible, as is the case in the study of the removal of trace elements described in [22], however our experimental data only covers these two cases. Subsequently we briefly describe a numerical scheme for a more complete set of equations.

4.1. Approximate solution method

Neglecting the $\mathcal{O}(\delta_3)$ term in Eq. (14c) and applying the relation $\phi_2 = 1 - \phi_1$, we obtain a simple relation between the concentrations

$$\hat{c}_2 = \frac{1 - \phi_1 \hat{c}_1}{1 - \phi_1}. \quad (20)$$

If $\delta_3 \sim 10^{-2}$ we expect this reduction to result in errors of the order 1%.

Upon neglecting terms of order $\mathcal{O}(\delta_1, \delta_2)$, the mass balance for the carrier fluid becomes

$$\frac{\partial}{\partial \hat{x}} (\hat{u} \hat{c}_2) = 0, \quad (21)$$

subject to $\hat{u} \hat{c}_2 = 1$ at $\hat{x} = 0$ (this is the reduced form of condition (15b) after also neglecting δ_3). This trivially leads to

$$\hat{u} \hat{c}_2 = 1 \Rightarrow \hat{u} = \frac{1}{\hat{c}_2} = \frac{1 - \phi_1}{1 - \phi_1 \hat{c}_1}. \quad (22)$$

After combining Eqs. (14a), (22) and (20) and neglecting terms of order $\mathcal{O}(\delta_1, \delta_2)$, we obtain

$$\frac{\partial}{\partial \hat{x}} \left(\frac{(1 - \phi_1) \hat{c}_1}{1 - \phi_1 \hat{c}_1} \right) = -\frac{\partial \hat{q}}{\partial \hat{t}}, \quad (23)$$

which must be solved along with

$$\frac{\partial \hat{q}}{\partial \hat{t}} = \hat{c}_1^m (1 - \hat{q})^n - \delta_7 \hat{q}^n. \quad (24)$$

The pressure is determined by integrating

$$-\frac{\partial \hat{p}}{\partial \hat{x}} = \hat{u}, \quad (25)$$

(neglecting terms of order $\mathcal{O}(\delta_4, \delta_6)$). Using $\hat{p}(\hat{L}, \hat{t}) = 0$ we find

$$\hat{p}(\hat{x}, \hat{t}) = \int_{\hat{x}}^{\hat{L}} \hat{u}(\hat{\xi}, \hat{t}) d\hat{\xi}, \quad (26)$$

therefore the system has now been reduced to solving for only two unknowns, \hat{c}_1 and \hat{q} .

The reduced system, Eqs. (23,24), may be solved exactly for certain combinations of m and n . This involves introducing a function $F(\eta) = (1 - \phi_1) \hat{c}_1 / (1 - \phi_1 \hat{c}_1)$ where the travelling

wave co-ordinate $\eta = \hat{x} - \hat{s}(\hat{t})$, and $d\hat{s}/d\hat{t} = v$ is constant, see [21, 22, 26]. In the travelling wave co-ordinate system the equations may be integrated immediately. The derivation for the most common physical cases $m = 1$ and $n = 1, 2$ is detailed in the Supplementary Information (these values correspond to the experiments discussed in §5). The solution for the contaminant concentration $\hat{c}_1(\hat{x}, \hat{t})$ may be written in implicit form

$$\left(1 + \delta_7^{1/n}\right) (\hat{t} - \hat{t}_{1/2}) - (\hat{x} - \hat{L}) = \hat{Y}_{mn}(\hat{c}_1), \quad (27)$$

where

$$\hat{Y}_{11}(\hat{c}_1) = \frac{1 + \delta_7}{1 + \phi_1 \delta_7} \left(\ln \left| \frac{\hat{c}_1}{1 - \hat{c}_1} \right| - \phi_1 \ln \left| \frac{(2 - \phi_1)\hat{c}_1}{1 - \phi_1 \hat{c}_1} \right| \right), \quad (28a)$$

$$\hat{Y}_{12}(\hat{c}_1) = \frac{1 + \sqrt{\delta_7}}{\sqrt{\delta_7} (1 + \sqrt{\gamma})} \left(\ln \left| \frac{\hat{c}_1}{1 - \hat{c}_1} \right| - \gamma \ln \left| \frac{(2 - \gamma)\hat{c}_1}{1 - \gamma \hat{c}_1} \right| \right), \quad (28b)$$

and

$$\gamma = \left(\frac{1 + \phi_1 \sqrt{\delta_7}}{1 + \sqrt{\delta_7}} \right)^2. \quad (28c)$$

The remaining variables may be calculated from the relations

$$\hat{c}_2 = \frac{1 - \phi_1 \hat{c}_1}{1 - \phi_1}, \quad \hat{q} = \frac{(1 - \phi_1)\hat{c}_1}{(1 + \delta_7^{1/n})(1 - \phi_1 \hat{c}_1)}, \quad \hat{u} = \frac{1 - \phi_1}{1 - \phi_1 \hat{c}_1}, \quad \hat{p} = \int_{\hat{x}}^{\hat{L}} \hat{u}(\hat{\xi}, \hat{t}) d\hat{\xi}. \quad (29)$$

Setting $\hat{x} = \hat{L}$ in (27) provides the breakthrough curve

$$\hat{t} = \hat{t}_{1/2} + \frac{\hat{Y}_{mn}(\hat{c}_{1b})}{1 + \delta_7^{1/n}}, \quad (30)$$

with $\hat{c}_{1b}(\hat{t}) = \hat{c}_1(\hat{L}, \hat{t})$. The fact that this solution depends only on δ_1 and ϕ_1 , indicates that the most important parameters affecting breakthrough are the ratio of adsorption to desorption, the feed contaminant concentration and volume fraction.

4.2. Dimensional solutions

The solutions given by equations (27–30) define the concentration of contaminant, carrier fluid, amount adsorbed, velocity and pressure. All of these solutions are novel and represent a breakthrough in the understanding of the adsorption of large quantities of a fluid. Given that many practitioners prefer to work in dimensional form we now present the solutions in terms of the original variables.

The concentration of the contaminant is

$$\left(1 + \delta_7^{1/n}\right) \frac{t - t_{1/2}}{\mathcal{T}} - \frac{x - L}{\mathcal{L}} = Y_{mn}(c_1), \quad (31)$$

where

$$Y_{11}(c_1) = \frac{1 + \delta_7}{1 + \phi_1 \delta_7} \left(\ln \left| \frac{c_1}{c_{10} - c_1} \right| - \phi_1 \ln \left| \frac{(2 - \phi)c_1}{c_{10} - \phi_1 c_1} \right| \right), \quad (32a)$$

$$Y_{12}(c_1) = \frac{1 + \sqrt{\delta_7}}{\sqrt{\delta_7} (1 + \sqrt{\gamma})} \left(\ln \left| \frac{c_1}{c_{10} - c_1} \right| - \gamma \ln \left| \frac{(2 - \gamma)c_1}{c_{10} - \gamma c_1} \right| \right), \quad (32b)$$

and γ defined by equation (28c).

The carrier gas concentration, adsorbed amount, and velocity are then

$$c_2(x, t) = \frac{p_a}{R_g T} - c_1(x, t), \quad q(x, t) = \frac{q_{max}(1 - \phi_1)c_1(x, t)}{(1 + \delta_7^{1/n})(c_{10} - \phi_1 \hat{c}_1)}, \quad u(x, t) = \frac{(1 - \phi_1)u_0 c_{10}}{c_{10} - \phi_1 c_1(x, t)}, \quad (33a)$$

while the pressure is given by

$$p(x, t) = p_a + \beta \int_x^L u(\xi, t) d\xi. \quad (34)$$

Finally, evaluating Eq. (31) at $x = L$ yields the dimensional breakthrough models for the Langmuir model, $(m, n) = (1, 1)$

$$t = t_{1/2} + \frac{\mathcal{T}}{1 + \phi_1 \delta_7} \left(\ln \left| \frac{c_{1b}}{c_{10} - c_{1b}} \right| - \phi_1 \ln \left| \frac{(2 - \phi_1) c_{1b}}{c_{10} - \phi_1 c_{1b}} \right| \right), \quad (35a)$$

and the Sips model with $(m, n) = (1, 2)$

$$t = t_{1/2} + \frac{\mathcal{T}}{\sqrt{\delta_7}(1 + \sqrt{\gamma})} \left(\ln \left| \frac{c_{1b}}{c_{10} - c_{1b}} \right| - \gamma \ln \left| \frac{(2 - \gamma) c_{1b}}{c_{10} - \gamma c_{1b}} \right| \right), \quad (35b)$$

where $c_{1b} = c_1(L, t)$ is the breakthrough concentration of component 1, $\mathcal{T} = 1/(k_a c_{10} q_{max}^{n-1})$, $\delta_7 = 1/(K c_{10})$ and $\gamma = ((1 + \phi_1 \sqrt{\delta_7})/(1 + \sqrt{\delta_7}))^2$.

In the limit of trace amounts of contaminant, $\phi_1 \rightarrow 0$, equation (35a) reduces to

$$t = t_{1/2} + \frac{1}{k_a c_{10}} \ln \left| \frac{c_{1b}}{c_{10} - c_{1b}} \right| \quad \Rightarrow \quad c_{1b} = \frac{c_{10}}{1 + \exp(k_a c_{10}(t_{1/2} - t))}, \quad (36)$$

which is the result of Myers *et al.* [21]. Setting $\phi_1 \rightarrow 0$, equation (35b) with $\mathcal{T} = 1/(k_a c_{10} q_{max})$, $\gamma = (1 + \sqrt{\delta_7})^{-2}$ reproduces the $(m, n) = (1, 2)$ result of Aguarales *et al.* [22].

4.3. Numerical solution

Due to the non-linear form of Eq. (14d) the numerical integration of the full model is not straightforward. However, following the work of [26] we may develop a numerical scheme neglecting only the parameters $\delta_3, \delta_4, \delta_6$, which have a maximum size of order 10^{-2} (so we retain any larger parameters). Eq. (14d) then becomes Eq. (25) and Eq. (14c) can be rearranged to Eq. (20). Substituting the expression for \hat{c}_2 into Eq. (14b) and combining with Eq. (14a) yields

$$\frac{\partial \hat{u}}{\partial \hat{x}} = \phi_1 \left(\delta_1 \frac{\partial \hat{c}_1}{\partial \hat{t}} + \frac{\partial}{\partial \hat{x}} (\hat{u} \hat{c}_1) - \delta_2 \frac{\partial^2 \hat{c}_1}{\partial \hat{x}^2} \right) = -\phi_1 \frac{\partial \hat{q}}{\partial \hat{t}}. \quad (37)$$

A boundary condition for \hat{u} is obtained by combining conditions (15b, 15a) at $\hat{x} = 0$ along with the relation (20) to determine $\hat{u}(0, \hat{t}) = 1$. Integrating Eq. (37) then gives

$$\hat{u}(\hat{x}, \hat{t}) = 1 - \phi_1 \int_0^{\hat{x}} \frac{\partial \hat{q}}{\partial \hat{t}}(\hat{\xi}, \hat{t}) d\hat{\xi} = 1 - \phi_1 \hat{Q}_{acc}(\hat{x}, \hat{t}), \quad (38)$$

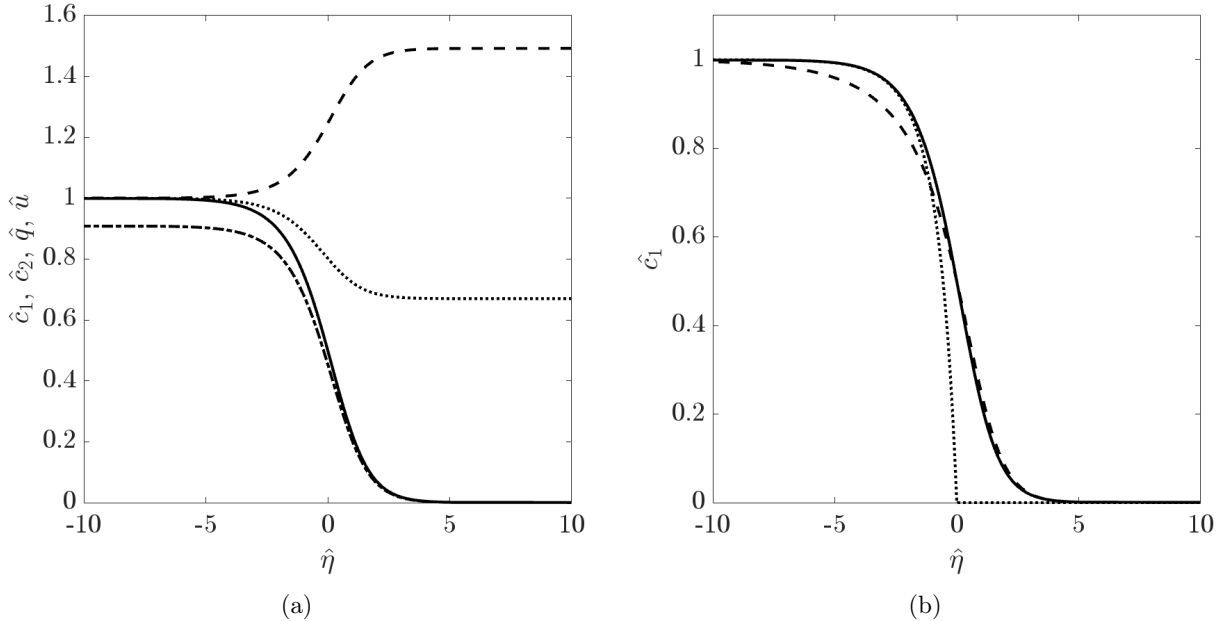


Figure 2: Profiles of (a) the contaminant concentration \hat{c}_1 (solid line), the carrier fluid concentration \hat{c}_2 (dashed line), adsorbed amount \hat{q} (dashed-dotted line) and flow velocity \hat{u} (dotted line) for the case $(m, n) = (1, 1)$ as a function of the travelling wave coordinate $\hat{\eta}$ with $\phi_1 = 0.33$ and $\delta_7 = 0.1$; (b) the contaminant concentration \hat{c}_1 : solid and dashed lines correspond to the cases $(1, 1)$ and $(1, 2)$. For comparison, the linear driving force solution (LDF) presented in [26] is shown as a dotted line.

where $\hat{Q}_{acc}(\hat{x}, \hat{t})$ represents the rate of change of accumulated contaminant within the column. Substituting this into Eq. (25) and integrating yields

$$\hat{p}(\hat{x}, \hat{t}) = \hat{L} - \hat{x} - \phi_1 \int_{\hat{x}}^{\hat{L}} \hat{Q}_{acc}(\hat{\xi}, \hat{t}) d\hat{\xi}, \quad (39)$$

where we have used $\hat{p} = 0$ at $\hat{x} = \hat{L}$.

Within this approximation the problem reduces to solving Eqs. (14a) and (14e), along with the integral (38), to find \hat{c}_1 , \hat{q} and \hat{u} , while \hat{c}_2 and \hat{p} become passive variables that may be obtained afterwards. For the numerical integration of (14a) and (14e) we use an explicit Euler marching scheme, while the spatial derivatives from the advection and diffusion terms in (14a) are discretised via a first order upwind scheme and a second order central differences scheme, respectively.

4.4. Discussion of solutions

In this section we show and discuss the analytical solutions obtained in section 4.1 and compare them with the numerical solutions using the approach described in section 4.3. We also discuss the differences between the solutions of the current model and the corresponding ones when the flow velocity is constant.

4.4.1. Travelling wave solutions

In Figure 2a we show the profiles of \hat{c}_1 , \hat{c}_2 , \hat{q} and \hat{u} from the travelling wave solution as a function of the travelling wave coordinate η for the case $(m, n) = (1, 1)$. The concentration

profile for the contaminant is characterised by a wave that tends to the inlet value, $c_1 = 1$, as $\eta \rightarrow -\infty$ and decreases gradually to 0 as $\eta \rightarrow +\infty$. Similarly, the adsorbed fraction tends to its constant equilibrium value near the inlet, in this case $\hat{q} \approx 0.88$, and to zero near the wave front where the adsorbent material is still clean of contaminant (i.e. $\hat{q} = 0$). In the region of the column where the adsorbent is full of contaminant the gas velocity is highest and it decreases towards the clean region of the column, indicating that adsorption slows down the propagation of the gas mixture through the column. The profiles for the case (1, 2) (not shown) show equivalent behaviour with some qualitative differences in the concentration profiles.

In Figure 2b we show the concentration profiles for the contaminant for the cases $(m, n) = (1, 1)$ and $(1, 2)$, along with the profile obtained by the LDF model, equation (8), which is derived in [26]. The profiles for $(m, n) = (1, 1)$ and $(1, 2)$ are almost identical for $\eta > 0$ while for $\eta < 0$ the case (1, 2) shows lower concentrations of contaminant than the case $(m, n) = (1, 1)$. This is consistent with the results reported in Aguarales et. al. [22] for the removal of trace amounts. The profile corresponding to the LDF model shows a very rapid decrease to zero at $\eta = 0$, this is related to its physical deficiency: near the wave front $c, q \rightarrow 0$ and hence $\partial q / \partial t = k_L(q_e - q) \rightarrow k_L q_e$, that is adsorption rate takes its highest possible value where there is virtually no contaminant.

4.4.2. Breakthrough curves

An accurate description of the breakthrough curve is crucial to the understanding of the mass transfer dynamics in column adsorption. The travelling wave solutions developed in section §4.1 present a simple method to describe the behaviour throughout the column and specifically the breakthrough. However, before applying the approximate solutions to real breakthrough data it is important to verify their accuracy. Here we do this through comparison with the numerical solution.

In Figure 3 we compare the analytical expressions for breakthrough of \hat{c}_1 , \hat{c}_2 , \hat{q} and \hat{u} with those obtained numerically using the procedure described in §4.3. In the case $n = 1$ the results are barely distinguishable, for the case $n = 2$ slight differences may be observed close to the end of the wave. We note that first breakthrough occurs at a slightly later time for the $n = 1$ case and the curve $\hat{c}_1(\hat{L}, \hat{t})$ is slightly steeper. This suggests a lower (non-dimensional) average velocity of the carrier fluid, which is consistent with the contaminant wave speed $\hat{v} = 1 + \delta_7^{1/n}$ when $\delta_7 < 1$. The general good agreement provides confidence in the accuracy of the analytical solution.

4.4.3. Large mass removal and velocity variation

The non-dimensional solutions (29, 30) indicate a dependence on only two parameters, ϕ_1, δ_7 . In Fig. 4 we examine the effect of varying ϕ_1 on the outlet concentration and velocity, with $\delta_7 = 5$ fixed. The curves correspond to the values $\phi_1 = 0.14, 0.21, 0.45, 0.69$, which are taken from the experiments of [14] and described in §5. Also shown is the fixed velocity case, which corresponds to $\phi_1 = 0$. We observe that the $\phi_1 = 0$ case shows a wider spread at breakthrough than the other curves: the slopes decrease in width with increasing ϕ_1 . Note, even at 14% there is a significant difference from the fixed velocity result (we will discuss this later). In Fig. 4b we show the evolution of velocity at the outlet. For times sufficiently earlier than $\hat{t}_{1/2}$ all contaminant is captured and the outlet velocity $\hat{u}(\hat{L}, \hat{t}) = 1 - \phi_1$ (this may be seen by taking the limit $\hat{c}_1 \rightarrow 0$ in Eq. (29)).

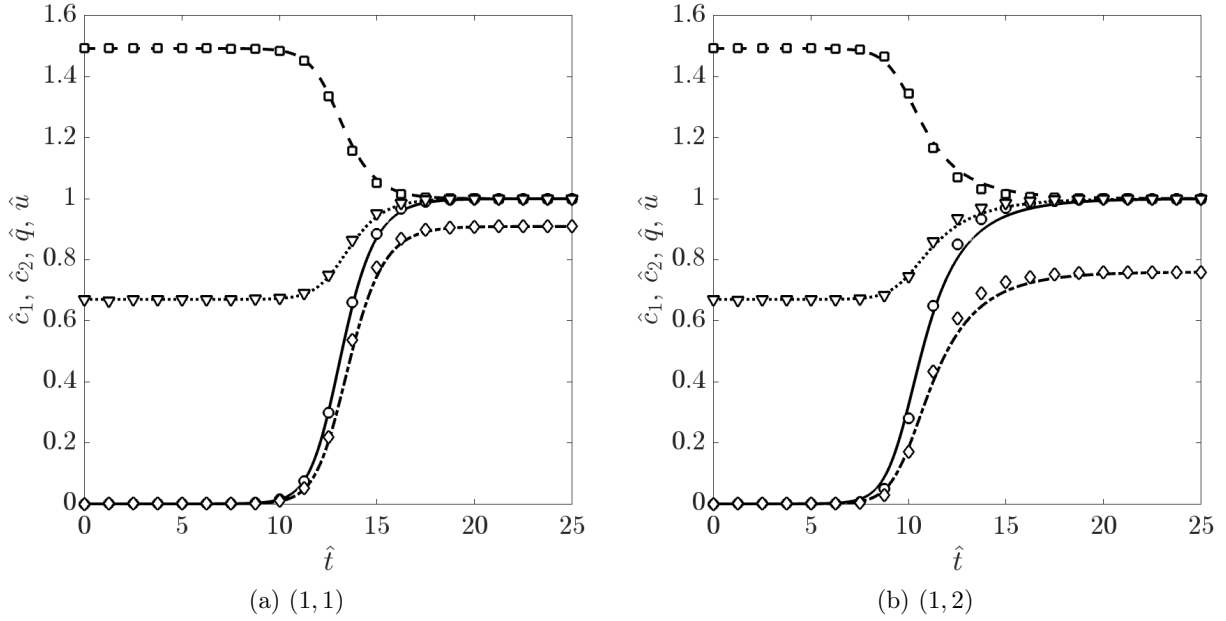


Figure 3: Evolution of the dependent variables at $\hat{x} = \hat{L}$ for different combinations $m = 1, n = 1, 2$. Lines refer to the analytical solutions developed in §4.1, symbols refer to the numerical solutions described in §4.3. The contaminant and carrier concentrations \hat{c}_1 and \hat{c}_2 , adsorbed amount \hat{q} and flow velocity \hat{u} are represented, respectively, by solid lines and circles, dashed lines and squares, dashed-dotted lines and diamonds, and dotted lines and triangles. The parameters have been set to $\phi_1 = 0.33$ and $\delta_7 = 0.1$. The remaining parameters in the numerical solutions are $\hat{L} = 15$, $\delta_1 = 10^{-3}$, $\delta_2 = 0.01$, $\delta_3 = 0.01$, $\delta_4 = 10^{-3}$, $\delta_5 = 0.1$, and $\delta_6 = 10^{-5}$, which are consistent with the experimental data for CO₂ capture of [9], see §5.

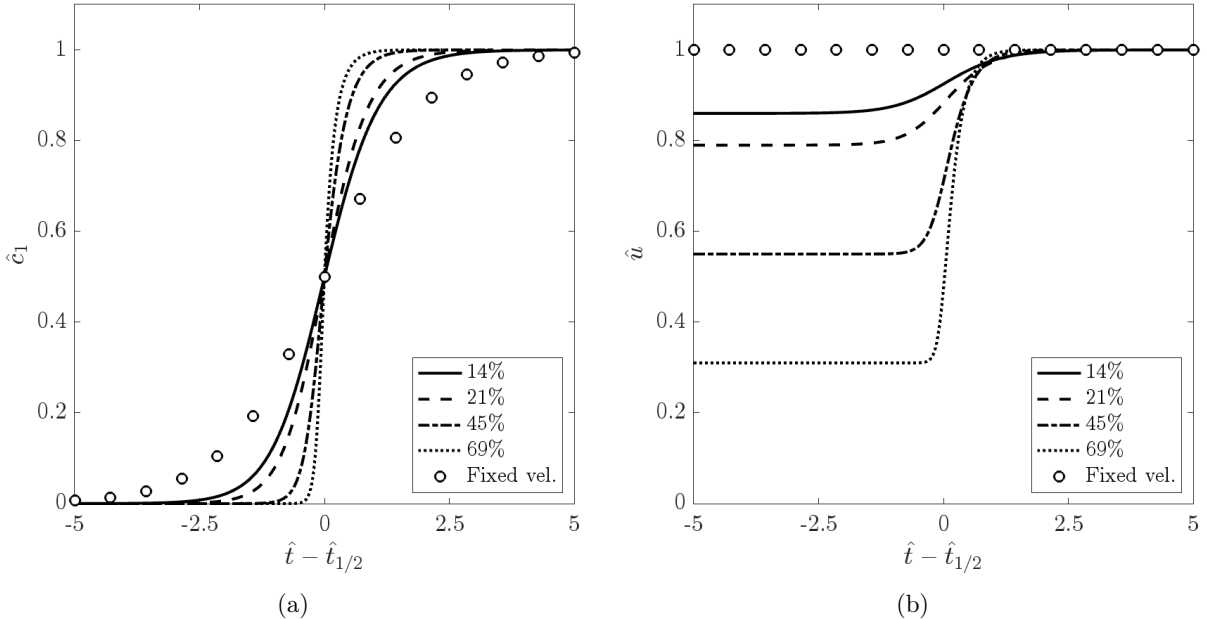


Figure 4: Variation of the contaminant breakthrough curve, (30), and fluid velocity at the outlet, (29), for different volume fractions and $m = n = 1$. The fixed velocity curves correspond to setting $\phi_1 = 0$. The adsorption-to-desorption ratio is $\delta_7 = 5$. All parameter values are consistent with the experiments of [14], see Table 4.

5. Application to CO₂ capture

In this section, we validate the variable-velocity model against experimental data from Monazam *et al.* [9] and Delgado *et al.* [14].

5.1. Parameter values

Delgado *et al.* [14] provided column breakthrough data for CO₂ adsorption onto silicate pellets at four different volumetric percentages of CO₂ (14%, 21%, 45% and 69%, corresponding to their runs 10, 12, 13 and 14). The values of the relevant thermophysical parameters extracted from their original work are listed in Table 1. The dispersion coefficient has been approximated using the experimental chart of Levenspiel [29] which relates the inverse Bodenstein number with the Reynolds number of the flow in a packed bed. An estimate of the initial concentrations is obtained from the corresponding temperature and pressure measurements using the ideal gas law. The parameter values for q_{max} and K were found by fitting (11) to the isotherm data of [14]: this calculation is described in the Supplementary Material. Note that the isotherm fitting process also indicates the kinetics of the adsorption process (physisorption or chemisorption) and, in the case of chemisorption, the order of the reaction. Since the best fit of the data of [14] is obtained with $(m, n) = (1, 1)$ this mechanism could be either physical or chemical (*i.e.* a chemical reaction with kinetic orders 1). In the Supplementary Material we note that at room temperature CO₂ molecules are adsorbed by Van der Waals forces inside the micropores of the silicalite structure [30–32], consequently we may assume that the (1,1) behaviour in this case corresponds to physisorption.

Table 1: Material properties and operating conditions from the column adsorption experiments in [14]. Each number of run refers to the original number in [14].

Property	Symbol	Units	Value			
Run			10	12	13	14
CO ₂ vol. fraction	ϕ_1	-	0.14	0.21	0.45	0.69
Inlet CO ₂ conc.	c_{10}	mol/m ³	5.436	8.086	17.22	26.15
Inlet He conc.	c_{20}	mol/m ³	33.392	30.419	21.045	11.749
Final ad. fraction	$q_{e,exp}$	mol/kg	0.28	0.38	0.73	1.08
Max. ad. fraction	q_{max}	mol/kg	4.975	4.664	4.595	4.845
Inlet velocity ($\times 10^{-3}$)	u_0	m/s	3.223	3.328	3.443	2.764
Pressure ($\times 10^4$)	p_0	Pa	9.62	9.54	9.48	9.39
Column length	L	m		0.163		
Column radius	R	m		0.008		
Void fraction	ϵ	-		0.52		
Particle density	ρ_a	kg/m ³		1070		
Bulk density	ρ_b	kg/m ³		513.6		
CO ₂ molar mass	M_1	kg/mol		0.044		
He molar mass	M_2	kg/mol		0.004		
Particle diameter	d_p	m		1.4×10^{-3}		
Dispersion coef.	D	m ² /s		9.03×10^{-6}		
Temperature	T	°C		25		
Gas viscosity	μ_g	mPa·s		0.0192		
Eq. constant	K	m ³ /mol		0.01096		
Partial orders	m, n	-		1,1		

Monazam *et al.* performed column adsorption experiments [9] for CO₂ capture on PEI modified silica in an N₂ stream. The values of the relevant thermophysical parameters extracted from their original work are listed in Table 2. Two different temperatures and two different volumetric percentages of CO₂ (16.6% and 33.3%) were studied. The dispersion coefficient was obtained using the expression $D = 1.44 \times 10^{-5}/\epsilon$, see [26]. Since this coefficient is approximate, it has been assumed to be constant with temperature. The inlet concentrations were calculated using the ideal gas law. The value of q_{max} , K and the orders m, n were determined from the isotherm data of [33] for batch adsorption with the same adsorbate-adsorbent system. The calculations are described in detail in the Supplementary Material. From their data it appears that the adsorption mechanism changes with temperature, at $T = 40^\circ\text{C}$ the best fit to the isotherm occurs with $n = 2$, $m = 1$ while $m = n = 1$ fits the 70°C data. This switch in behaviour can be explained via specific physical/chemical mechanisms (see Supplementary Material).

Table 2: Operating conditions and parameter values from [9, 33]. Values separated by a dash refer to different volume fractions.

Property	Symbol	Units	Value	
Temperature	T	$^{\circ}\text{C}$	40	70
CO ₂ volume fraction	ϕ_1	-	0.333	0.166 - 0.333
Inlet CO ₂ conc.	c_{10}	mol/m^3	12.96	5.90 - 11.83
Inlet N ₂ conc.	c_{20}	mol/m^3	25.96	29.62 - 23.69
Final ad. frac.	$q_{e,\text{exp}}$	mol/kg	1.99	2.743 - 2.761
Partial orders	m, n	-	1, 2	1, 1
Max. ad. frac.	q_{max}	mol/kg	2.37	3.04 - 2.91
Eq. constant	K	$\text{m}^{3m}\text{kg}^{n-1}\text{mol}^{1-m-n}$	2.13	1.59
Gas viscosity	μ_g	$\text{mPa}\cdot\text{s}$	0.0185	0.0198
Column length	L	m		0.254
Column radius	R	m		0.07
Void fraction	ϵ	-		0.3
Particle density	ρ_a	kg/m^3		900
Bulk density	ρ_b	kg/m^3		630
CO ₂ molar mass	M_1	kg/mol		0.044
N ₂ molar mass	M_2	kg/mol		0.028
Particle diameter	d_p	m		1.5×10^{-4}
Dispersion coef.	D	m^2/s		4.8×10^{-5}
In. fluid velocity	u_0	m/s		0.0944
Pressure	p_a	Pa (Atm)		101325 (1)

5.2. Results of the fitting to the breakthrough data

The analysis of the isotherm data in the Supplementary Material determines the parameters q_{max} , K and the orders m , n , so the only remaining unknown is the adsorption coefficient k_a . Evaluating (31) at $x = L$ yields the breakthrough curves

$$Y_{11}(c_{1b}(t)) = \frac{1 + \delta_7}{\mathcal{T}}(t - t_{1/2}) \quad (40)$$

$$Y_{12}(c_{1b}(t)) = \frac{1 + \sqrt{\delta_7}}{\mathcal{T}}(t - t_{1/2}) \quad (41)$$

for $(m, n) = (1, 1)$ (Langmuir model) and $(m, n) = (1, 2)$, respectively. The functions Y_{11} , Y_{12} are defined by (32a)-(32b) and the value of $\delta_7 = 1/(Kc_{10})$ is known. Note the breakthrough curves (40)-(41) are linear functions in $t - t_{1/2}$ where the slope depends on the unknown k_a through $\mathcal{T} = 1/(k_a c_{10} q_{max}^{n-1})$. This permits a straightforward fitting procedure to determine k_a based on measuring how the experimental values of $Y_{mn}(c_{1b}(t))$ deviate from the theoretical linear profile. The fitting procedure is an extension of the one used in [22] for the constant velocity model.

Noting that the adsorption process studied in Delgado *et al.* [14] corresponds to a (1, 1) model in Fig. 5a we compare the predictions of equation (40) with the experimental Dataset 14, which has a volume fraction of CO₂ of 69% ($\phi_1 = 0.69$). The data points on the graph are generated by plotting $Y_{11}(c_{1b})/(1 + \delta_7)$ using the experimental values of $c_{1b}(t)$ versus the

times $t - t_{1/2}$, where $t_{1/2} = 2314\text{s} = 0.642$ hours. The solid line corresponds to the linear fit obtained using the `fit` function from the Matlab curve fitting toolbox. Fig. 5b shows the prediction using the constant velocity model (i.e., equation (40) with $\phi = 0$). Comparison of Figs. 5a and 5b demonstrate that the variable velocity model provides a much more accurate fit to the experimental data than the constant velocity model, which clearly deviates from the linear profile.

Repeating the fitting for all Runs detailed in Table 1 we obtain the results shown in Table 3. For Run 14 we observe that the variable velocity model has an $R^2 = 0.994$ and SSE of 0.01 while the values for the constant velocity model are 0.94, 4.8. Since the SSE refers to a logarithmic function of the experimental data its size is not so important, rather the important feature is that the variable velocity value is nearly five hundred times smaller than the constant velocity value. Although it is obvious from the graphs, Table 3 provides quantitative evidence that the constant velocity model is the most accurate when $\phi_1 = 0.69$. Reducing the volume fraction reduces the difference between the results: for the lowest value $\phi_1 = 0.14$ the SSE is only a factor 17 less than the $\phi_1 = 0$ result. In all cases the variable velocity model has a lower SSE and higher R^2 than the constant velocity result.

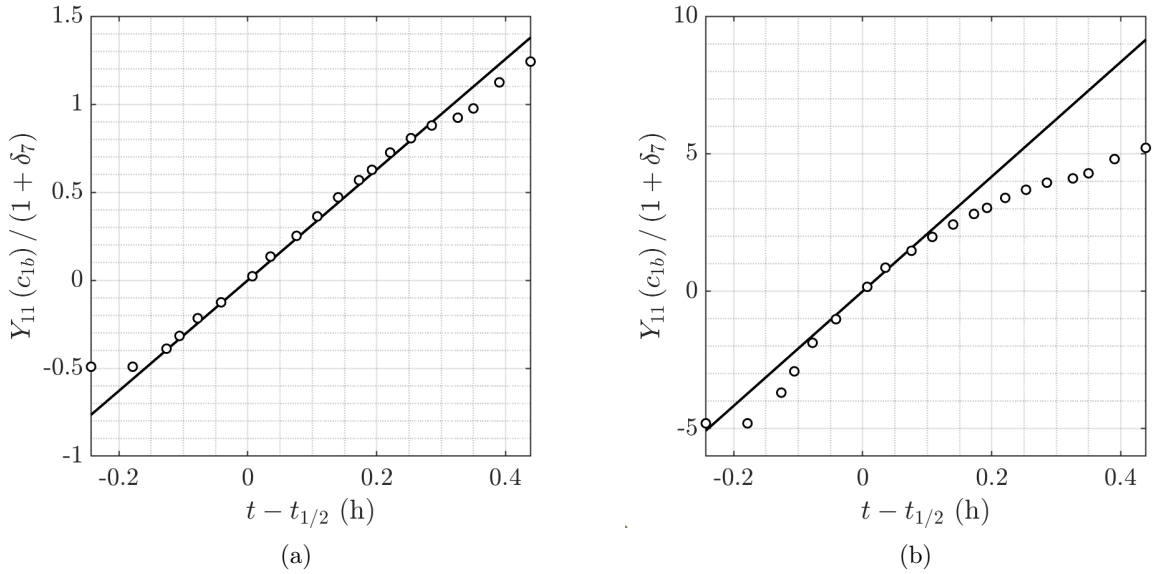


Figure 5: Dataset 14 of Delgado *et al.* [14], where the experimental data points are shown in the form $Y_{11}(c_{1b}) / (1 + \delta_7)$ against time $t - t_{1/2}$. The solid line is a straight line passing through the origin with a slope $1/\mathcal{T}$. On panel (a), Y_{11} is calculated for the variable velocity case with $\phi = 0.69$. On panel (b), Y_{11} is calculated for the constant velocity case, obtained by setting $\phi = 0$.

Table 3: Comparison between the fitting to Delgado *et al.* [14] breakthrough data of the $(m, n) = (1, 1)$ variable velocity model (equation (35a)) and the $(m, n) = (1, 1)$ constant velocity model.

Parameter	Value			
Run	10	12	13	14
ϕ_1 (-)	0.14	0.21	0.45	0.69
Variable velocity				
k_a ($\times 10^{-4}$) ($\text{m}^3\text{mol}^{-1}\text{s}^{-1}$)	1.341	0.971	0.592	0.334
SSE	0.667	1.251	0.102	0.010
R-squared	0.9433	0.9110	0.9746	0.9942
Constant velocity				
k_a ($\times 10^{-3}$) ($\text{m}^3\text{mol}^{-1}\text{s}^{-1}$)	0.472	0.374	0.268	0.221
SSE	11.375	28.540	9.259	4.800
R-squared	0.9248	0.8681	0.8993	0.9395

Table 4: Results obtained from the fitting to Delgado *et al.* [14] breakthrough data of the model with $(m, n) = (1, 1)$ (equation (35a)). The only fitting parameter is k_a , the rest are obtained using the values in Table 1.

Parameter	Value			
Run	10	12	13	14
ϕ_1 (-)	0.14	0.21	0.45	0.69
k_a ($\times 10^{-4}$) ($\text{m}^3\text{mol}^{-1}\text{s}^{-1}$)	1.341	0.971	0.592	0.334
k_d ($\times 10^{-2}$) (s^{-1})	1.223	0.886	0.539	0.304
\mathcal{T} (s)	1371.62	1272.97	981.74	1145.54
\mathcal{L} ($\times 10^{-2}$) (m)	0.4891	0.7438	1.283	1.731
\mathcal{P} ($\times 10^{-2}$) (Pa)	1.893	2.937	4.936	5.055
δ_1 ($\times 10^{-3}$)	1.106	1.755	3.794	5.465
δ_2	0.573	0.376	0.218	0.162
δ_3 ($\times 10^{-7}$)	1.968	3.079	5.207	5.383
δ_4 ($\times 10^{-3}$)	4.137	3.938	2.992	1.418
δ_5	1.791	2.924	9.000	24.48
δ_6 ($\times 10^{-4}$)	1.313	1.342	1.820	1.739
δ_7	16.769	11.273	5.294	3.486

The analytical solutions presented in Section 4.1 were derived assuming that some of the dimensionless parameters of the model are typically small in column adsorption processes. In Table 4 we show the value of these parameters along with k_a , k_d and the resulting values of the time, length, and pressure scales, for the data of [14]. The orders of magnitude of δ_1 , δ_3 , δ_4 and δ_6 are very small (between 10^{-7} and 10^{-3}). Although δ_5 is $\mathcal{O}(10)$, the product $\delta_4\delta_5 = \mathcal{O}(10^{-2})$, which is consistent with the model assumptions. In this example the column is working at a relatively low concentration for the adsorbent capacity. Thus, δ_7 is high, meaning that desorption is significant for most of the process. The value of δ_2 is relatively high because of the low velocity of the process. However, it is still low enough for the assumptions of the model to hold.

In previous analytical work on the removal of trace amounts it has been stressed that the adsorption coefficient, k_a , must remain constant with respect to concentration, [6, 21, 34], otherwise the solution method is invalid. However, it is well-known that k_a may vary with quantities such as temperature, pressure or flow rate. Here, the removal of large quantities of the fluid results in variations in both pressure and velocity. The effect of the velocity u on mass transfer parameters has previously been reported in the literature, see [35], prompting various experimental correlations that define k_a as a function of u . In Table 4 the reduction in k_a is approximately proportional to the reduction of $1 - \phi_1$, which coincides with the change in velocity (between $[1 - \phi_1, 1]$) suggesting the possibility of a linear variation $k_a \propto u$. We also note that as $\phi_1 \rightarrow 0$ the velocity variation tends to zero, which is then consistent with a fixed k_a for the removal of trace amounts.

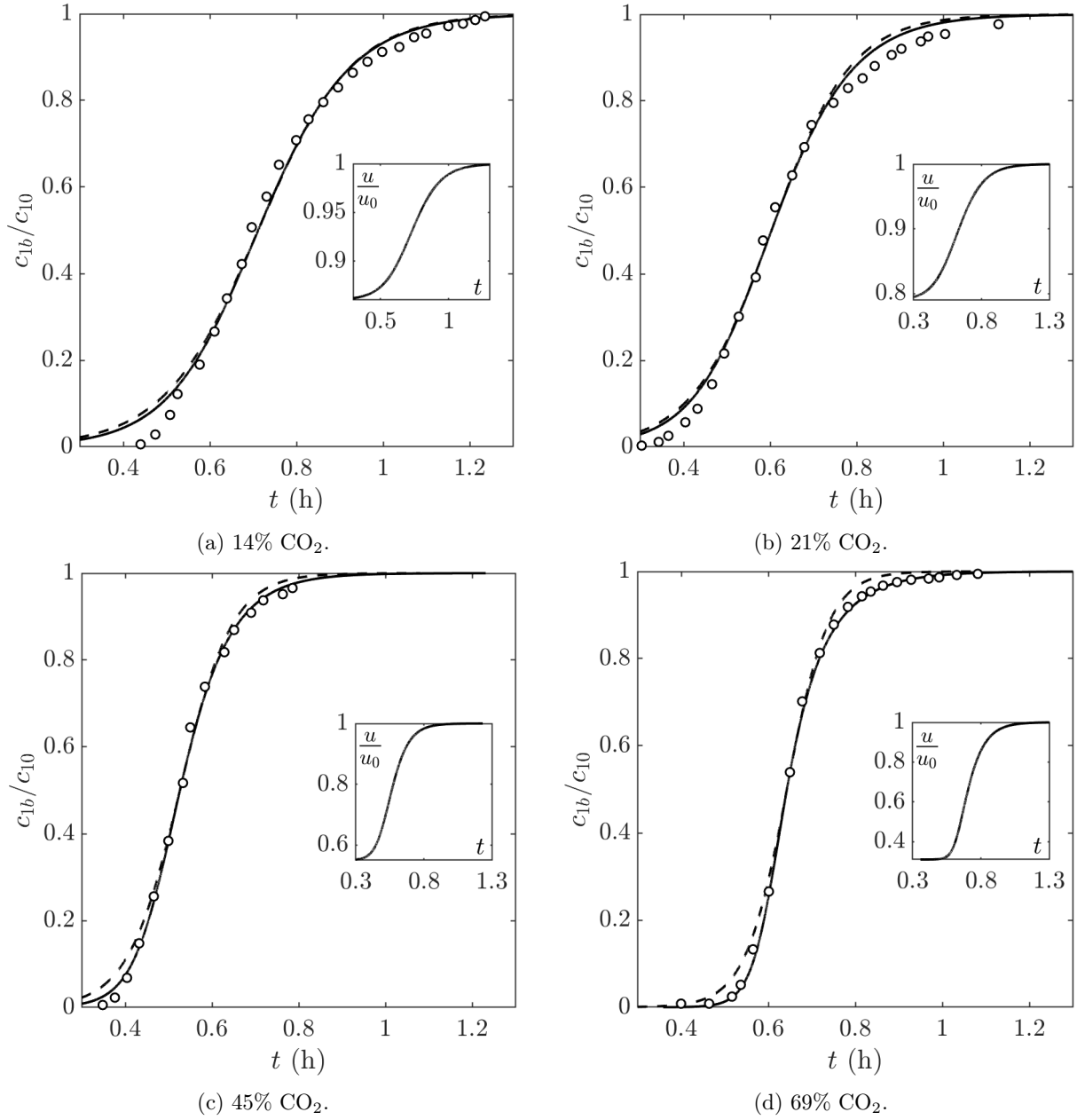


Figure 6: Fitting of the model accounting for $(m, n) = (1, 1)$ to the breakthrough data reported by Delgado *et al.* [14] with a range of CO₂ volumetric percentages ϕ_1 at the inlet of the column (runs 10, 12, 13 and 14 in Table 1). The constant velocity model (dashed line) is retrieved when setting $\phi_1 \rightarrow 0$ in Eq. (35a). In each figure, the inset shows the evolution of the flow velocity at the outlet as per Eq. (33a).

Whilst the linear form is an excellent way to understand the experimental data, the more standard procedure is to plot $c_b(t)$. In Figure 6 we plot the breakthrough data for the four cases of Runs 10, 12, 13, 14 and compare with the constant velocity model. A key observation here is that in this format, for the low concentration cases $\phi_1 = 0.14, 0.21$ the differences between the variable and constant velocity results are virtually indistinguishable. This indicates that if we

carry out a fitting based on this format it would be difficult to identify the correct model. From the linear format of Figure 5 it is clear that the variable velocity model is the correct one and therefore the value of k_a calculated by this method should be the more accurate. Both models miss a number of points, particularly when $\phi_1 = 0.21$, this could be due to some experimental error. For the high concentration results the variable velocity model captures almost all data points exactly while the constant velocity model reduces in accuracy.

We stress that for the low concentration results the close proximity of the variable and constant velocity curves does not imply that the results are equivalent. Rather it demonstrates that with parameter values adjusted appropriately the incorrect model may appear to be a good approximation. This may also be understood through Figure 4 which shows that, with all other quantities held constant the non-dimensional breakthrough curves vary significantly between the $\phi_1 = 0, 0.14$ cases. The difference in the form of the breakthrough curves is due to the second term in square brackets of equation (28a) which is proportional to ϕ_1 . The difference therefore increases with increasing ϕ_1 , however the scale of the difference changes due to the factor $1/(1 + \phi_1\delta_7)$ outside the brackets, which will magnify differences for small ϕ_1 . In dimensional form, equation (35a) introduces an additional factor $\tau = 1/(k_a c_{10})$, so any magnification of differences can be reduced by choosing a higher value of k_a (we note that in Tables 3, 4 k_a decreases with increasing ϕ_1). Consequently, the standard form of presenting breakthrough results may be a poor choice for fitting since it permits the incorrect model to appear accurate and the calculated value of k_a will not reflect the correct value of the adsorbent-adsorbate system. The linear form appears to be a more robust and accurate method.

We now analyse the data of Monazam *et al.* [9] for $T = 40^\circ C$ which is shown in the Supplementary Material to follow a $(m, n) = (1, 2)$ chemisorption model. In Figure 7a we compare the prediction of equation (41) with the experimental data. The data points are generated by plotting $Y_{12}(c_{1b})/(1 + \sqrt{\delta_7})$ computed with the outlet experimental values of $c_{1b}(t)$ against $t - t_{1/2}$. The linear fit is obtained by using the `fit` function from the Matlab curve fitting toolbox. In Figure 7b we show the analogous results obtained with the constant velocity model (setting $\phi_1 = 0$ in (41)). The variable velocity model captures the majority of data points at early times while the constant velocity model shows a poor agreement in this region. For large times the data is more scattered and both models give a relatively poor fit, however the deviations are clearly larger in the constant velocity model.

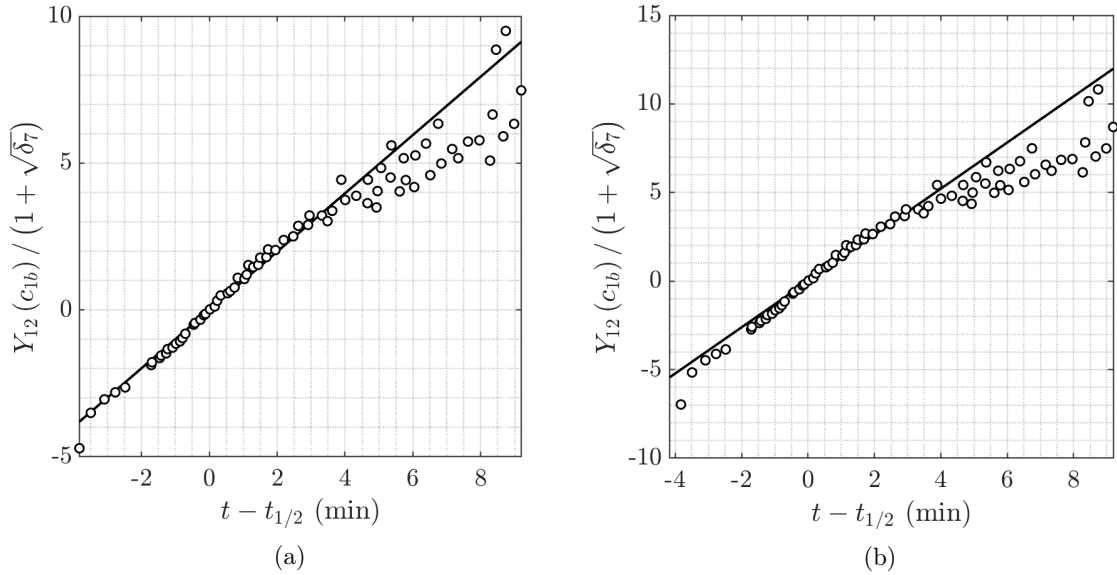


Figure 7: Linear fitting of Monazam *et al.* [9] data at 40°C using equation (41). On panel (a), Y_{12} is calculated for the variable velocity case with $\phi_1 = 0.333$. On panel (b), Y_{12} is calculated for the constant velocity case, $\phi_1 = 0$. The value of \mathcal{T} is retrieved from the inverse of the slope of the line.

The results of the fitting process for Figure 7 are shown in the first column of Table 5. While the R^2 values both indicate a good fit, the SSE value is three times higher for the constant velocity model. We also show the results of fitting to the 70°C data, which is modelled by a (1,1) reaction or physisorption. Again the R^2 values are close and for the case of $\phi_1 = 0.166$ the SSEs have a similar magnitude.

In Figure 7 it is apparent that the variable velocity model is more accurate for the case $T = 40^\circ\text{C}$ data, $\phi_1 = 0.333$. However, when plotting the standard $c_b(t)$ form of the breakthrough, shown in Figure 8, there is no noticeable difference between the two curves, although the k_a predicted for the constant velocity case is 30% higher than the variable velocity one. This confirms our assertion that fitting to the linear form is more robust than to the standard form of the breakthrough curve.

Table 5: Results of the fitting procedure for Monazam *et al.* [9] breakthrough data at 40°C and 70°C.

Parameter	Value		
ϕ_1 (-)	0.333	0.166	
T (°C)	40	70	
Partial orders	(1,2)	(1,1)	
Variable velocity ($\phi_1 > 0$)			
k_a ($\times 10^{-4}$) ($\text{m}^3\text{kg}^{n-1}\text{mol}^{-n}\text{s}^{-1}$)	5.388	6.230	7.088
SSE	2.865	1.297	27.412
R-squared	0.9857	0.9831	0.9081
Constant velocity ($\phi_1 = 0$)			
k_a ($\times 10^{-4}$) ($\text{m}^3\text{kg}^{n-1}\text{mol}^{-n}\text{s}^{-1}$)	7.074	7.392	7.673
SSE	8.482	2.882	31.126
R-squared	0.9762	0.9746	0.9130

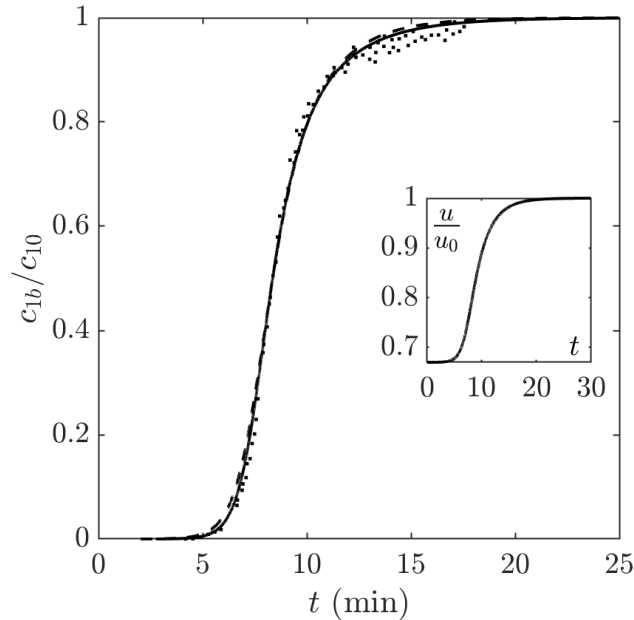


Figure 8: The dots correspond to the breakthrough data from Monazam *et al.* [9] at 40°C. The solid and dashed lines are the breakthrough curves from the variable and constant velocity models, respectively, for $(m, n) = (1, 2)$ with k_a obtained from the linear fit (see Table 5).

In Figure 9 we present the breakthrough curves for Monazam’s data at 70°C. As suggested by the SSE and R^2 values in Table 5, the fitting of both variable and constant velocity models is good: the relatively low R^2 is a result of the scatter of the many data points for larger times. In this case both models show similar results and a much smaller difference in predicted k_a values than with the data of [14].

Table 6: Results obtained from fitting to the experimental data of Monazam *et al.* [9] at 40°C and 70°C. The only fitting parameter is k_a , the rest are obtained using the values in Table 2.

Parameter	Value		
ϕ_1 (-)	0.333		0.166
T (°C)	40	70	
Partial orders	(1,2)	(1,1)	
k_a ($\times 10^{-4}$) ($\text{m}^3\text{kg}^{n-1}\text{mol}^{-n}\text{s}^{-1}$)	5.388	6.230	7.088
k_d ($\times 10^{-4}$) ($\text{kg}^{n-1}\text{mol}^{1-n}\text{s}^{-1}$)	2.532	3.930	4.471
\mathcal{T} (s)	60.43	135.71	239.29
\mathcal{L} ($\times 10^{-2}$) (m)	1.486	2.265	1.907
\mathcal{P} (Pa)	896.47	1246.81	1049.69
δ_1 ($\times 10^{-3}$)	2.60	1.94	0.92
δ_2 ($\times 10^{-2}$)	3.420	2.459	2.921
δ_3 ($\times 10^{-2}$)	0.885	1.231	1.036
δ_4 ($\times 10^{-3}$)	2.925	2.436	3.046
δ_5	0.784	0.784	0.313
δ_6 ($\times 10^{-6}$)	5.673	3.100	1.836
δ_7	0.036	0.053	0.107

The results of the fitting and calculated parameters and scales are shown in Table 6. The value of k_d has been calculated as $k_d = k_a/K$. Parameters δ_1 and δ_4 are both small, with an order of magnitude of 10^{-3} . In this example adsorption strongly dominates and δ_7 is small. Note that δ_2 , δ_3 and δ_6 are all less than 0.1, which validates the assumptions made when deriving the analytical solutions from section 4.1.

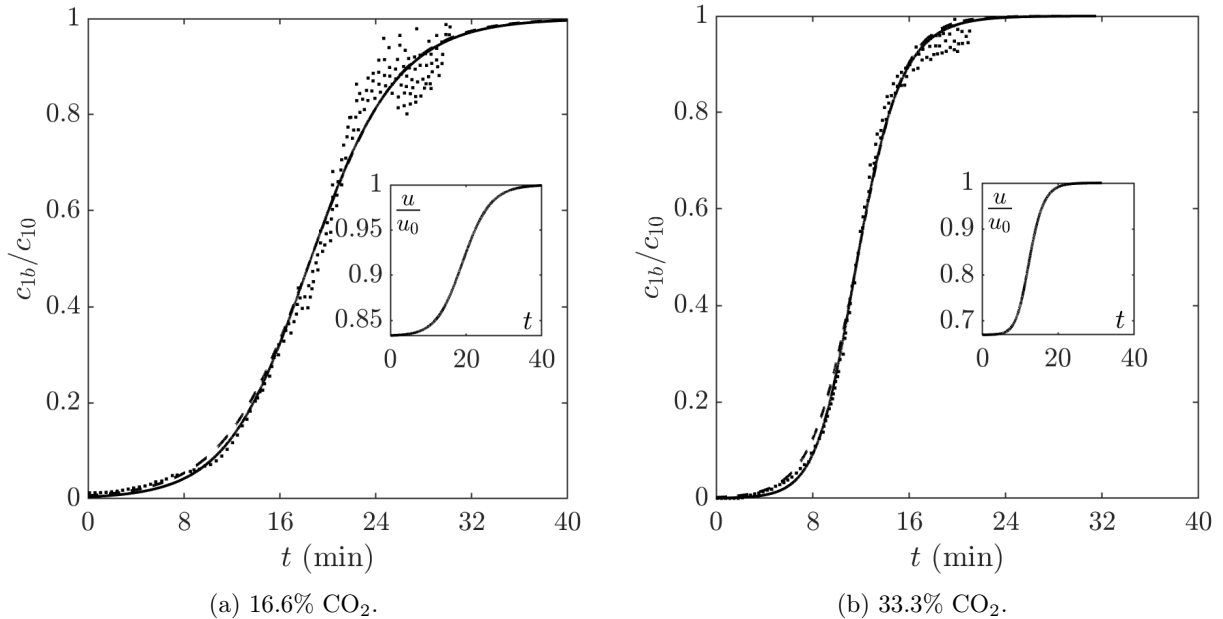


Figure 9: Fitting of the model to the breakthrough data reported by Monazam *et al.* [9] at 30 standard L/min and 70 °C with different volumetric percentages at the inlet of the column. Solid line: (1, 1) variable velocity model (equation (35a)); dashed line: (1, 1) constant velocity model. The constant velocity model is retrieved when setting $\phi_1 \rightarrow 0$ in Eq. (35a). In each figure, the inset shows the evolution of the flow velocity at the outlet as per Eq. (33a).

We observe that, for the data at 70°C in Table 6 where we have two sets of results, the value of k_a decreases by a factor of 0.88 when $1 - \phi_1$ decreases by a factor 0.8, suggesting an almost linear correlation between k_a and $1 - \phi_1$ and hence with u . This trend is consistent with our previous analysis of Delgado’s data.

6. Conclusion

In this paper we have developed a mathematical model that describes the removal of large quantities of contaminant from a fluid mixture via adsorption. Comparison of numerical and approximate analytical solutions demonstrated the accuracy of the approximate solutions. Comparison of the approximate solutions with experimental data demonstrated the accuracy of the method. Specifically we examined the capture of CO₂ with volume fractions ranging from 14 to 69%, finding excellent agreement in all cases.

The key result of the paper is the set of analytical solutions describing the concentration, pressure, velocity and amount adsorbed throughout the column. All of these solutions are novel and represent a breakthrough in the understanding of the adsorption of large quantities of a fluid. The non-dimensional solution indicated that the most important parameters affecting the breakthrough form are the ratio of adsorption to desorption, the feed contaminant concentration and volume fraction. The dimensional solution shows how this shape is stretched in the time domain, which then adds the adsorption rate, maximum possible adsorption amount and form of chemical reaction to the list of controlling parameters.

Expressions for the breakthrough curve were provided in an implicit form

$$t = t_{1/2} + mY(c), \quad (42)$$

where the form of Y depends on the chemical reaction and volume fraction. Here we derived solutions for the case of physisorption or a 1, 1 chemical reaction (1 contaminant molecule reacts with 1 adsorbent) and also a 1, 2 reaction. More complicated reactions could be described following the same solution method. The standard route is to describe breakthrough concentration as a function of time, via the explicit form $c = f(t)$. Plotting the former, as a straight line graph, t versus $Y(c)$, against experimental data provides a clear picture of which model (i.e. which chemical reaction, large mass or trace removal) is applicable. Plotting results in the explicit form, the differences between model and data are not always clear, making it easier to accept an incorrect model. This assertion was confirmed through two groups of experimental data, in both cases good agreement could be obtained between trace amount of contaminant result and the large mass one when plotting c as a function of time. However, when using the linear form it was clear that the trace amount model did not correctly predict the behaviour and so could not be trusted.

Existing models of trace removal rely on the adsorption coefficient, k_a , remaining constant with respect to concentration. For example, the Langmuir mass loss term has $\partial q/\partial t \propto k_a c(q_{max} - q)$. To obtain an analytical solution integration is carried out assuming c , q are variable and k_a is constant. If solutions show that $k_a = k_a(c)$ then the integrations are invalid and the solution no longer holds. Instead the kinetic equation should be rewritten, for example with $k_a c^m$, such that k_a is independent of c , and a new integration carried out. However, it is well-known that the adsorption rate may vary with pressure and flow rate. Removing trace amounts these do not vary significantly, removing large amounts both may vary. Consequently we observed a decrease in k_a with increasing volume fraction of contaminant (corresponding to a reduction in velocity and pressure with respect to the trace amount model).

Future work will concentrate on expanding the solutions to different chemical reactions, whenever appropriate experimental data is available to verify the results as well as investigating the relation between velocity and adsorption coefficient. While we have focussed on parameter regimes relevant to adsorption columns, so motivating model reductions, the models may apply to a variety of sorption phenomena with different parameters, different reductions and different behaviour. This could be a rich vein for subsequent investigations.

Declaration of Competing Interest

The authors declare that they have no known competing financial interests or personal relationships that could have appeared to influence the work reported in this paper.

Acknowledgements

This publication is part of the research projects PID2020-115023RB-I00 and TED2021-131455A-I00 (funding T. Myers and F. Font) financed by MCIN/AEI/ 10.13039/501100011033/, by “ERDF A way of making Europe” and by “European Union NextGenerationEU/PRTR”. A. Valverde acknowledges support from the Margarita Salas UPC postdoctoral grants funded by the Spanish Ministry of Universities with European Union funds - NextGenerationEU. T. Myers and M. Calvo-Schwarzwalder thank CERCA Programme/Generalitat de Catalunya for institutional support. This work is supported by the Spanish State Research Agency, through the Severo Ochoa and Maria de Maeztu Program for Centres and Units of Excellence in R&D (CEX2020-001084-M). F. Font is a Serra-Hunter fellow from the Serra-Hunter Programme of

the Generalitat de Catalunya. F. Font gratefully acknowledges the SRG programme (2021-SGR-01045) of the Generalitat de Catalunya (Spain).

References

- [1] G. S. Bohart, E. Q. Adams, Some aspects of the behaviour of charcoal with respect to chlorine, *Journal of the American Chemical Society* 42 (3) (1920) 523–544. doi:10.1021/ja01448a018.
- [2] N. Amundson, A note on the mathematics of adsorption in beds, *J. Phys. Chem.* 52 (7) (1948) 1153–1157. doi:10.1021/j150463a007.
- [3] Y. Yoon, J. Nelson, Application of gas adsorption kinetics I. A theoretical model for respirator cartridge service life, *American Industrial Hygiene Association Journal* 45(8) (1984) 509–516. doi:10.1080/15298668491400197.
- [4] M. S. Shafeeyan, W. M. A. W. Daud, A. Shamiri, A review of mathematical modeling of fixed-bed columns for carbon dioxide adsorption, *Chemical Engineering Research and Design* 92 (5) (2014) 961–988. doi:10.1016/j.cherd.2013.08.018.
- [5] S. Li, S. Deng, L. Zhao, R. Zhao, M. Lin, Y. Du, Y. Lian, Mathematical modeling and numerical investigation of carbon capture by adsorption: Literature review and case study, *Applied Energy* 221 (2018) 437–449. doi:10.1016/j.apenergy.2018.03.093.
- [6] T. G. Myers, Is it time to move on from the Bohart-Adams model for column adsorption?, submitted to *International Communications in Heat and Mass Transfer* (2024). URL <https://ssrn.com/abstract=4528144>
- [7] Y.-C. Chiang, Y.-J. Chen, C.-Y. Wu, Effect of relative humidity on adsorption breakthrough of CO₂ on activated carbon fibers, *Materials* 10 (11) (2017). doi:10.3390/ma10111296.
- [8] Q. Huang, C. H. Niu, A. K. Dalai, Dynamic study of butanol and water adsorption onto oat hull: Experimental and simulated breakthrough curves, *Energy & Fuels* 33 (10) (2019) 9835–9842. doi:10.1021/acs.energyfuels.9b01662.
- [9] E. R. Monazam, J. Spenik, L. J. Shadle, Fluid bed adsorption of carbon dioxide on immobilized polyethylenimine (PEI): Kinetic analysis and breakthrough behavior, *Chemical Engineering Journal* 223 (2013) 795–805. doi:10.1016/j.cej.2013.02.041.
- [10] R. F. P. M. Moreira, J. L. Soares, G. L. Casarin, A. E. Rodrigues, Adsorption of CO₂ on hydrotalcite-like compounds in a fixed bed, *Separation Science and Technology* 41 (2) (2006) 341–357. doi:10.1080/01496390500496827.
- [11] R. Sabouni, H. Kazemian, S. Rohani, Mathematical modeling and experimental breakthrough curves of carbon dioxide adsorption on metal organic framework CPM-5, *Environmental Science & Technology* 47 (16) (2013) 9372–9380. doi:10.1021/es401276r.

- [12] M. S. Shafeeyan, W. M. A. W. Daud, A. Shamiri, N. Aghamohammadi, Modeling of carbon dioxide adsorption onto ammonia-modified activated carbon: Kinetic analysis and breakthrough behavior, *Energy & Fuels* 29 (10) (2015) 6565–6577. doi:10.1021/acs.energyfuels.5b00653.
- [13] M. Bastos-Neto, A. Moeller, R. Staudt, J. Böhm, R. Gläser, Dynamic bed measurements of co adsorption on microporous adsorbents at high pressures for hydrogen purification processes, *Separation and Purification Technology* 77 (2) (2011) 251–260. doi:https://doi.org/10.1016/j.seppur.2010.12.015.
- [14] J. A. Delgado, M. A. Uguina, J. L. Sotelo, B. Ruíz, Fixed-bed adsorption of carbon dioxide–helium, nitrogen–helium and carbon dioxide–nitrogen mixtures onto silicalite pellets, *Separation and Purification Technology* 49 (1) (2006) 91–100. doi:10.1016/j.seppur.2005.08.011.
- [15] Y. Ding, E. Alpay, Equilibria and kinetics of CO₂ adsorption on hydrotalcite adsorbent, *Chemical Engineering Science* 55 (17) (2000) 3461–3474. doi:10.1016/S0009-2509(99)00596-5.
- [16] N. Casas, J. Schell, R. Pini, M. Mazzotti, Fixed bed adsorption of CO₂/H₂ mixtures on activated carbon: experiments and modeling, *Adsorption* 18 (2012) 143–161. doi:10.1007/s10450-012-9389-z.
- [17] S. Ergun, A. A. Orning, Fluid flow through randomly packed columns and fluidized beds, *Industrial & Engineering Chemistry* 41 (6) (1949) 1179–1184. doi:10.1021/ie50474a011.
- [18] T. L. Dantas, F. M. T. Luna, I. J. Silva, D. C. de Azevedo, C. A. Grande, A. E. Rodrigues, R. F. Moreira, Carbon dioxide–nitrogen separation through adsorption on activated carbon in a fixed bed, *Chemical Engineering Journal* 169 (1) (2011) 11–19. doi:10.1016/j.cej.2010.08.026.
- [19] T. L. P. Dantas, A. E. Rodrigues, R. F. P. M. Moreira, Separation of carbon dioxide from flue gas using adsorption on porous solids, in: G. Liu (Ed.), *Greenhouse Gases*, IntechOpen, Rijeka, 2012, Ch. 3, pp. 57–80. doi:10.5772/31917.
- [20] T. G. Myers, F. Font, M. G. Hennessy, Mathematical modelling of carbon capture in a packed column by adsorption, *Applied Energy* 278 (2020) 115565. doi:10.1016/j.apenergy.2020.115565.
- [21] T. G. Myers, A. Cabrera-Codony, A. Valverde, On the development of a consistent mathematical model for adsorption in a packed column (and why standard models fail), *International Journal of Heat and Mass Transfer* 202 (2023) 123660. doi:10.1016/j.ijheatmasstransfer.2022.123660.
- [22] M. Agualeles, E. Barrabés, T. Myers, A. Valverde, Mathematical analysis of a Sips-based model for column adsorption, *Physica D: Nonlinear Phenomena* 448 (2023) 133690. doi:10.1016/j.physd.2023.133690.

- [23] A. Valverde, A. Cabrera-Codony, M. Calvo-Schwarzwalder, T. Myers, Investigating the impact of adsorbent particle size on column adsorption kinetics through a mathematical model, *International Journal of Heat and Mass Transfer* 218 (2024) 124724. doi:10.1016/j.ijheatmasstransfer.2023.124724.
- [24] L. C. Auton, M. Aguares, A. Valverde, T. G. Myers, M. Calvo-Schwarzwalder, Analytical investigation into solute transport and sorption via intra-particle diffusion in the dual-porosity limit, submitted to *Applied Mathematical Modelling* (2024). URL <https://arxiv.org/abs/2311.10161>
- [25] T. G. Myers, A. Valverde, M. Aguares, M. Calvo-Schwarzwalder, F. Font, Modelling mass transfer from a packed bed by fluid extraction, *International Journal of Heat and Mass Transfer* 188 (2022) 122562. doi:10.1016/j.ijheatmasstransfer.2022.122562.
- [26] T. G. Myers, F. Font, Mass transfer from a fluid flowing through a porous media, *International Journal of Heat and Mass Transfer* 163 (2020) 120374. doi:10.1016/j.ijheatmasstransfer.2020.120374.
- [27] R. Mondal, S. Mondal, K. V. Kurada, S. Bhattacharjee, S. Sengupta, M. Mondal, S. Karmakar, S. De, I. M. Griffiths, Modelling the transport and adsorption dynamics of arsenic in a soil bed filter, *Chemical Engineering Science* 210 (2019) 115205. doi:10.1016/j.ces.2019.115205.
- [28] R. Sips, On the structure of a catalyst surface, *The Journal of Chemical Physics* 16 (5) (1948) 490–495. doi:10.1063/1.1746922.
- [29] O. Levenspiel, *Chemical Reaction Engineering*, 3rd Edition, John Wiley & Sons, Inc, 1999. URL <https://www.wiley.com/en-us/Chemical+Reaction+Engineering%2C+3rd+Edition-p-9780471254249>
- [30] L. Grajciar, J. Čejka, A. Zúkal, C. Otero Areán, G. Turnes Palomino, P. Nachtigall, Controlling the adsorption enthalpy of CO₂ in zeolites by framework topology and composition, *ChemSusChem* 5 (10) (2012) 2011–2022. doi:10.1002/cssc.201200270.
- [31] N. Jiang, M. Erdös, O. A. Moulton, R. Shang, T. J. Vlugt, S. G. Heijman, L. C. Rietveld, The adsorption mechanisms of organic micropollutants on high-silica zeolites causing s-shaped adsorption isotherms: An experimental and monte carlo simulation study, *Chemical Engineering Journal* 389 (2020) 123968. doi:10.1016/j.cej.2019.123968.
- [32] M. Santoro, F. Gorelli, J. Haines, O. Cambon, C. Levelut, G. Garbarino, Silicon carbonate phase formed from carbon dioxide and silica under pressure, *Proceedings of the National Academy of Sciences* 108 (19) (2011) 7689–7692. doi:10.1073/pnas.1019691108.
- [33] E. R. Monazam, L. J. Shadle, D. C. Miller, H. W. Pennline, D. J. Fauth, J. S. Hoffman, M. L. Gray, Equilibrium and kinetics analysis of carbon dioxide capture using immobilized amine on a mesoporous silica, *AIChE Journal* 59 (3) (2013) 923–935. doi:10.1002/aic.13870.

- [34] H. C. Croll, M. J. Adelman, S. J. Chow, K. J. Schwab, R. Capelle, J. Oppenheimer, J. G. Jacangelo, Fundamental kinetic constants for breakthrough of per- and polyfluoroalkyl substances at varying empty bed contact times: Theoretical analysis and pilot scale demonstration, *Chem. Eng. J.* 464 (2023) 142587. doi:10.1016/j.cej.2023.142587.
- [35] J. Puiggené, M. Larrayoz, F. Recasens, Free liquid-to-supercritical fluid mass transfer in packed beds, *Chemical Engineering Science* 52 (2) (1997) 195–212. doi:10.1016/S0009-2509(96)00379-X.

Supplementary Material

Modelling large mass removal in adsorption columns

T. G. Myers, M. Calvo-Schwarzwalder, F. Font, A. Valverde

1 Analytical approximation

1.1 Reduced model

Neglecting all terms deemed small through the non-dimensionalisation, the governing equations are

$$\frac{\partial}{\partial \hat{x}} (\hat{u} \hat{c}_1) = -\frac{\partial \hat{q}}{\partial \hat{t}}, \quad (1a)$$

$$\frac{\partial}{\partial \hat{x}} (\hat{u} \hat{c}_2) = 0, \quad (1b)$$

$$1 = \phi_1 \hat{c}_1 + (1 - \phi_1) \hat{c}_2, \quad (1c)$$

$$-\frac{\partial \hat{p}}{\partial \hat{x}} = \hat{u}, \quad (1d)$$

$$\frac{\partial \hat{q}}{\partial \hat{t}} = \hat{c}_1^m (1 - \hat{q})^n - \delta_7 \hat{q}^n. \quad (1e)$$

where ϕ_1 is the contaminant volume fraction and δ_7 is the adsorption-to-desorption ratio. The boundary and initial conditions are

$$1 = \hat{u}(0, \hat{t}) \hat{c}_1(0, \hat{t}), \quad \left. \frac{\partial \hat{c}_1}{\partial \hat{x}} \right|_{\hat{x}=\hat{L}} = 0, \quad \hat{c}_1(\hat{x}, 0) = 0, \quad (2a)$$

$$1 = \hat{u}(0, \hat{t}) \hat{c}_2(0, \hat{t}), \quad \left. \frac{\partial \hat{c}_2}{\partial \hat{x}} \right|_{\hat{x}=\hat{L}} = 0, \quad \hat{c}_2(\hat{x}, 0) = 1/(1 - \phi_1), \quad (2b)$$

$$\hat{p}(0, \hat{t}) = \Delta \hat{p}, \quad \hat{p}(\hat{L}, \hat{t}) = 0, \quad \hat{p}(\hat{x}, 0) = \hat{p}_{in}(\hat{x}), \quad (2c)$$

$$\hat{q}(\hat{x}, 0) = 0, \quad (2d)$$

with $\hat{p}_{in}(\hat{x}) = \Delta \hat{p}(0) (1 - \hat{x}/\hat{L})$. From this reduced formulation we can immediately determine \hat{c}_2 , \hat{u} , and \hat{p} in terms of \hat{c}_1 ,

$$\hat{c}_2 = \frac{1 - \phi_1 \hat{c}_1}{1 - \phi_1}, \quad \hat{u} = \frac{1}{\hat{c}_2} = \frac{1 - \phi_1}{1 - \phi_1 \hat{c}_1}, \quad \hat{p} = \int_{\hat{x}}^{\hat{L}} \hat{u}(\hat{\xi}, \hat{t}) d\hat{\xi}, \quad (3)$$

which reduces the problem to determining \hat{c}_1 and \hat{q} . Upon substituting \hat{u} in Eq. (1a) the equation for \hat{c}_1 becomes

$$\frac{\partial}{\partial \hat{x}} \left(\frac{(1 - \phi_1) \hat{c}_1}{1 - \phi_1 \hat{c}_1} \right) = -\frac{\partial \hat{q}}{\partial \hat{t}}, \quad (4)$$

which is coupled to the kinetic equation (1e).

1.2 Calculation of travelling wave solutions

The reduced system formed by Eqs. (1e) and (4) can be simplified using a common approach based on introducing a travelling wave coordinate. For this we define $\hat{\eta} = \hat{x} - \hat{s}(\hat{t})$, where $d\hat{s}/d\hat{t} = \hat{v} > 0$, and define

$$\frac{(1 - \phi_1)\hat{c}_1}{1 - \phi_1\hat{c}_1} =: \hat{F}(\hat{\eta}), \quad \hat{q}(\hat{x}, \hat{t}) =: \hat{G}(\hat{\eta}). \quad (5)$$

Equation (4) becomes

$$\frac{d\hat{F}}{d\hat{\eta}} = \hat{v} \frac{d\hat{G}}{d\hat{\eta}}, \quad (6)$$

which can be directly integrated to

$$\hat{F} = \hat{v}\hat{G}, \quad (7)$$

where the constant of integration has been chosen to be zero to satisfy $\hat{F}, \hat{G} \rightarrow 0$ as $\hat{\eta} \rightarrow \infty$, i.e., that no contaminant is present far ahead of the moving front. The kinetic equation (1e) becomes

$$-\hat{v} \frac{d\hat{G}}{d\hat{\eta}} = \left(\frac{\hat{F}}{1 - \phi_1 + \phi_1\hat{F}} \right)^m (1 - \hat{G})^n - \delta_7 \hat{G}^m. \quad (8)$$

Far behind the moving front, the process is expected to have reached an equilibrium state and therefore $\hat{F} \rightarrow \hat{F}_e$ and $\hat{G} \rightarrow \hat{G}_e$ as $\hat{\eta} \rightarrow -\infty$. Moreover, we expect $\hat{c}_1 \rightarrow 1$ far behind the moving front where the system is in equilibrium. Using this in the definition of \hat{F} , we find

$$\hat{F}_e = 1, \quad (9)$$

whereas taking the limit as $\hat{\eta} \rightarrow -\infty$ in Eq. (8) with $d\hat{G}/d\hat{\eta} \rightarrow 0$ yields

$$\hat{G}_e = \frac{1}{1 + \delta_7^{1/n}}, \quad (10)$$

which is the non-dimensional equilibrium value of \hat{q} (as specified in the main text). Taking the limit as $\hat{\eta} \rightarrow -\infty$ in Eq. (7) determines the wave velocity

$$\hat{v} = \frac{\hat{F}_e}{\hat{G}_e} = 1 + \delta_7^{1/n}. \quad (11)$$

Finally, it is left to solve Eq. (8), which can be combined with Eq. (7) to give a single ordinary differential equation for \hat{F} ,

$$-\frac{d\hat{F}}{d\hat{\eta}} = \left(\frac{\hat{F}}{1 - \phi_1 + \phi_1\hat{F}} \right)^m \left(1 - \frac{\hat{F}}{\hat{v}} \right)^n - \delta_7 \left(\frac{\hat{F}}{\hat{v}} \right)^n, \quad (12)$$

This equation must be solved numerically in general, but we can find analytical solutions for certain combinations of n and m which are of interest. As for where the front is defined, we define $\hat{\eta} = 0$ as the point where $\hat{c}_1 = 1/2$, hence

$$\hat{F}(0) = \hat{F}_{1/2} := \frac{1 - \phi_1}{2 - \phi_1}. \quad (13)$$

Upon defining the origin of the wave variable $\hat{\eta}$ in this way, we can write it explicitly as $\hat{\eta} = \hat{x} - \hat{L} - \hat{v}(\hat{t} - \hat{t}_{1/2})$, where $t_{1/2}$ is the (experimentally obtained) time when the outlet concentration is half the inlet value and $\hat{t}_{1/2} = t_{1/2}/\mathcal{T}$.

1.2.1 Case $m = 1, n = 1$

In this case, Eq. (12) may be written

$$-\frac{d\hat{F}}{d\hat{\eta}} = \frac{\hat{F}}{1 - \phi_1 + \phi_1\hat{F}} \left(1 - \frac{\hat{F}}{\hat{v}}\right) - \delta_7 \frac{\hat{F}}{\hat{v}} = \frac{a\hat{F}(1 - \hat{F})}{1 - \phi_1 + \phi_1\hat{F}}, \quad (14)$$

where $a = (1 + \phi_1\delta_7)/\hat{v} > 0$. Rearranging and splitting the fraction yields

$$-1 = \left[\frac{1 - \phi_1 + \phi_1\hat{F}}{a\hat{F}(1 - \hat{F})} \right] \frac{\partial\hat{F}}{\partial\hat{\eta}} = \left[\frac{1 - \phi_1}{a\hat{F}} + \frac{1}{a(1 - \hat{F})} \right] \frac{d\hat{F}}{d\hat{\eta}}. \quad (15)$$

This equation can be directly integrated to give

$$\mathcal{C} - \hat{\eta} = \frac{1 - \phi_1}{a} \ln(\hat{F}) - \frac{1}{a} \ln(1 - \hat{F}). \quad (16)$$

applying $\hat{F}(0) = \hat{F}_{1/2}$ determines the constant of integration to give the solution

$$-\hat{\eta} = \frac{1 - \phi_1}{a} \ln\left(\frac{\hat{F}}{\hat{F}_{1/2}}\right) - \frac{1}{a} \ln\left(\frac{1 - \hat{F}}{1 - \hat{F}_{1/2}}\right). \quad (17)$$

1.2.2 Case $m = 1, n = 2$

Equation (12) now can be rearranged to give

$$-\frac{d\hat{F}}{d\hat{\eta}} = \frac{\hat{F}}{1 - \phi_1 + \phi_1\hat{F}} \left(1 - \frac{\hat{F}}{\hat{v}}\right)^2 - \delta_7 \left(\frac{\hat{F}}{\hat{v}}\right)^2 = \frac{\hat{F}(1 - \hat{F})(a - \hat{F})}{a(1 - \phi_1 + \phi_1\hat{F})}, \quad (18)$$

with $a = \hat{v}^2/(1 - \phi_1\delta_7) = (1 + \sqrt{\delta_7})^2/(1 - \phi_1\delta_7)$. We may rewrite this as

$$-\frac{d\hat{\eta}}{a} = \left[\frac{1 - \phi_1 + \phi_1\hat{F}}{\hat{F}(1 - \hat{F})(a - \hat{F})} \right] d\hat{F}. \quad (19)$$

The value $a \geq 1$ for $\delta_7 \in [0, 1/\phi_1)$ and $a \leq -1/\phi_1$ for $\delta_7 > 1/\phi_1$.

Case i) $a = 1 + \omega^2 \geq 1$. Writing a in terms of $\omega^2 > 0$, the integration is simple. After replacing ω^2 and rearranging we obtain

$$-\hat{\eta} = (1 - \phi_1) \ln\left(\frac{\hat{F}}{\hat{F}_{1/2}}\right) - \frac{a}{a - 1} \ln\left(\frac{1 - \hat{F}}{1 - \hat{F}_{1/2}}\right) + \left(\phi_1 + \frac{1}{a - 1}\right) \ln\left(\frac{a - \hat{F}}{a - \hat{F}_{1/2}}\right), \quad (20)$$

where we have used $\hat{F}(0) = \hat{F}_{1/2}$.

Case ii) $a = -1/\phi_1 - \omega^2 = -\nu^2 < 0$. Writing a in terms of $-\nu^2$, we may follow the same route as for the previous calculation and obtain the same result, but note the final log term is now valid since both denominator and numerator are negative (for the case $a \geq 1$ they are both positive).

1.3 Final solutions

Equation (7) provides a simple relation between \hat{F} , \hat{G} . In terms of the original non-dimensional variables, \hat{c}_1, \hat{q} , this leads to

$$\hat{q} = \frac{(1 - \phi_1)\hat{c}_1}{(1 + \delta_7^{1/n})(1 - \phi_1\hat{c}_1)}. \quad (21)$$

Writing η in terms of the original variables \hat{c}_1 is defined implicitly by

$$(1 + \delta_7^{1/n})(\hat{t} - \hat{t}_{1/2}) - (\hat{x} - \hat{L}) = \hat{Y}_{mn}(\hat{c}_1), \quad (22)$$

where the expression of \hat{Y}_{mn} come from the right hand sides of either Eqs. (17, 20). Rearranging and replacing F the final expressions are

$$\hat{Y}_{11}(\hat{c}_1) = \frac{1 + \delta_7}{1 + \phi_1\delta_7} \left[\ln \left| \frac{\hat{c}_1}{1 - \hat{c}_1} \right| - \phi_1 \ln \left| \frac{(2 - \phi)\hat{c}_1}{1 - \phi_1\hat{c}_1} \right| \right], \quad (23a)$$

$$\hat{Y}_{12}(\hat{c}_1) = \frac{1 + \sqrt{\delta_7}}{\sqrt{\delta_7}(1 + \sqrt{\gamma})} \left[\ln \left| \frac{\hat{c}_1}{1 - \hat{c}_1} \right| - \gamma \ln \left| \frac{(2 - \gamma)\hat{c}_1}{1 - \gamma\hat{c}_1} \right| \right], \quad (23b)$$

and

$$\gamma = \left(\frac{1 + \phi_1\sqrt{\delta_7}}{1 + \sqrt{\delta_7}} \right)^2. \quad (23c)$$

The remaining quantities are determined by Eq. (3).

2 Isotherm study of CO₂ capture

2.1 CO₂ adsorption onto silicate pellets from helium stream

Delgado *et al.* [1] provide the isotherm obtained during their column experiments. The data points and fits using the Sips isotherm with ratios $m/n = 1$ and $m/n = 0.5$ are shown in Fig. 1. The parameters q_{max}, K obtained from the fitting of the isotherm are provided in Table 1. These values are used in the main document so that only one unknown remains in the fitting of the breakthrough data.

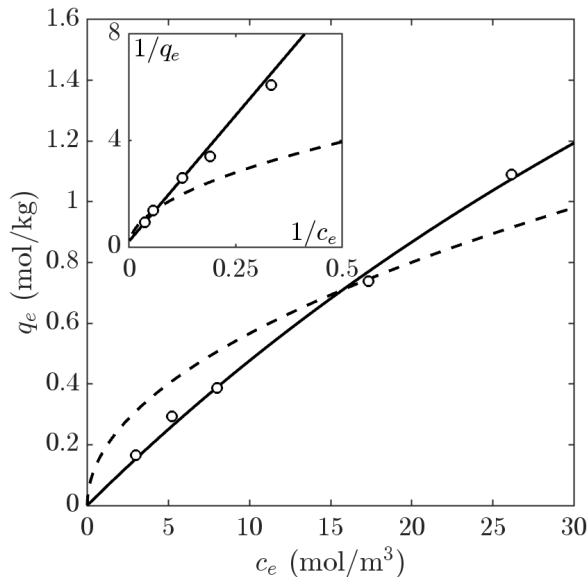


Figure 1: Fitting of the experimental isotherm data reported by Delgado *et al.* [1]. The solid line refers to $m/n = 1$ and the dashed line to $m/n = 0.5$. c_e refers to the inlet concentration at which equilibrium is reached in the column. Insets show $1/c_e$ vs $1/q_e$. As these isotherms are obtained via column adsorption experiments, we have $c_e = c_{10}$.

Table 1: Values of the isotherm parameters obtained from fitting the Sips isotherm to the experimental data reported by Delgado *et al.* [1].

Orders ratio	q_{max} (mol/kg)	K ($m^{3m}kg^{n-1}mol^{1-m-n}$)	SSE (mol^2/kg^2)	R-squared
$m/n = 0.5$	7.0×10^{11}	2.6×10^{-13}	0.0793	0.8598
$m/n = 1$	4.8224	0.01097	0.0024	0.9957

The ratio $m/n = 1$ shows excellent agreement with the isotherm data, whereas the ratio $m/n = 0.5$ clearly shows a poor fit. This is consistent with the adsorption mechanism of CO_2 on silicalite pellets. Near ambient temperature CO_2 molecules are adsorbed by Van der Waals forces inside the micropores of the silicalite structure, mainly by dispersion forces [2, 3, 4]. The Langmuir isotherm ($m/n = 1$ ratio) accounts for homogeneous adsorption of isolated molecules in the most favoured sites of the silicalite structure [5]. Consequently, in the main document we only employ $(m, n) = (1, 1)$ using the associated q_{max}, K values.

2.2 CO_2 capture onto PEI modified silica from N_2 stream

In Monazam *et al.* [6] equilibrium (batch) data is provided for CO_2 capture on PEI modified silica from N_2 . This is the same adsorbate-adsorbent system as studied in the column adsorption experiments of Monazam *et al.* [7]. In [6], only the isotherms at $40^\circ C$ and $100^\circ C$ are provided. However, they also provide the coefficients obtained from fitting the isotherms at $50^\circ C$, $60^\circ C$ and $80^\circ C$ with Freundlich and Langmuir isotherms. Since the fits with the Freundlich isotherm at $50^\circ C$ and $60^\circ C$ show good agreement (R-squared 0.992 and 0.989, respectively), we created

data points for these temperatures using Freundlich's coefficients in order to carry out a new fitting with the Sips isotherm accounting for $m/n = 1$ and $m/n = 0.5$. The results are shown in Figure 2.

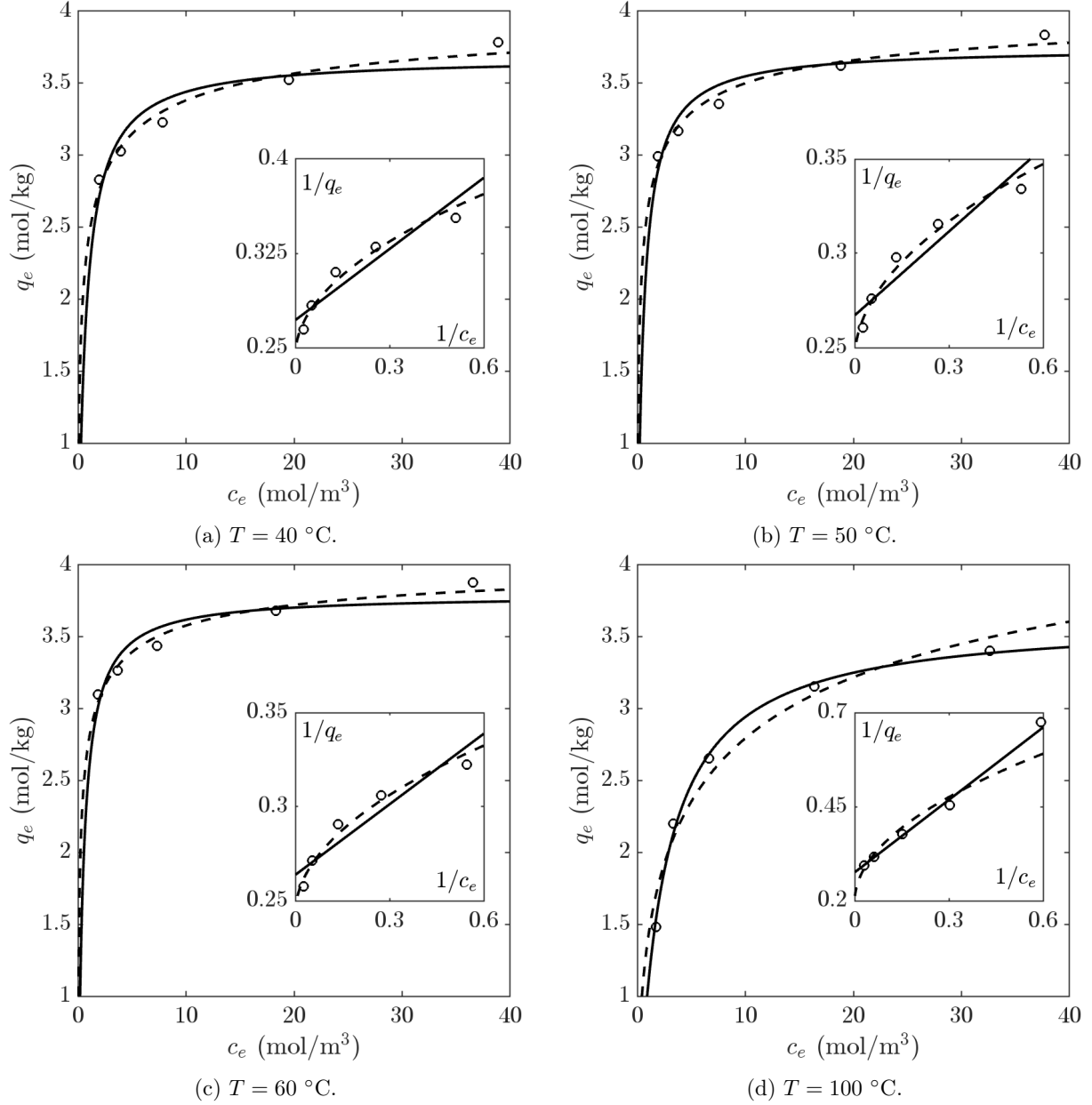


Figure 2: Fitting of the experimental isotherms reported by Monazam *et al.* [6] using the Sips isotherm. The solid line refers to $m/n = 1$ (Langmuir isotherm) and the dashed line to $m/n = 0.5$. The symbol c_e refers to the value of the concentration when equilibrium is reached inside the batch reactor. Insets show $1/c_e$ vs $1/q_e$.

The parameters obtained from the fitting of each isotherm are reported in Table 2.

Table 2: Parameters values obtained from fitting the Sips isotherm to the experimental batch data of Monazam *et al.* [6]. The subscript b in $q_{max,b}$ refers batch.

T ($^{\circ}\text{C}$)	40	50	60	100
$m = 1 \quad n = 2$				
$q_{max,b}$ (mol/kg)	4.114	4.113	4.119	5.077
K ($\text{m}^3\text{kg}/\text{mol}^2$)	2.128	3.275	4.400	0.150
SSE (mol^2/kg^2)	0.0189	0.0138	0.0122	0.0846
R-squared	0.9675	0.9701	0.9689	0.9642
$m = 1 \quad n = 1$				
$q_{max,b}$ (mol/kg)	3.679	3.745	3.791	3.629
K (m^3/mol)	1.440	1.801	2.111	0.429
SSE (mol^2/kg^2)	0.0752	0.0576	0.0496	0.0085
R-squared	0.8708	0.8751	0.8731	0.9964

Both Fig. 2 and the results in Table 2 show that the Sips isotherm with $m/n = 0.5$ fits the experimental data up to 60°C , whereas for 100°C the better fit occurs with $m/n = 1$. The equilibrium constant K increases from 40°C to 60°C , while $q_{max,b}$ remains approximately constant. The increase of K results in a steeper isotherm, which means that for a fixed c_e the equilibrium value q_e will also increase with temperature. However, there is a change in behaviour observable in the 100°C result, which shows a far lower K value (and consequently lower q_e values). In physisorption processes K is expected to decrease with temperature, since the intermolecular forces responsible for retaining the adsorbate molecules, weaken with increasing temperature. However, chemisorption processes may show an opposite trend when the enthalpy of reaction is positive.

In the main text we analyse breakthrough data at 70°C . The value of the equilibrium constant used in this case was calculated by extrapolation of the results at 80°C reported by [6], and the values obtained at 100°C from Fig. 2 using the Van't Hoff equation [8, 9].

The adsorbed fractions may differ between batch and column experiments, however, we expect the equilibrium constant K to be relatively constant between the two. Consequently we calculate q_{max} for column experiments using the Sips isotherm and substituting for K from the batch results and q_e from the column experiment.

References

- [1] José A. Delgado, María A. Uguina, José L. Sotelo, and Beatriz Ruíz. Fixed-bed adsorption of carbon dioxide–helium, nitrogen–helium and carbon dioxide–nitrogen mixtures onto silicalite pellets. *Separation and Purification Technology*, 49(1):91–100, 2006.
- [2] Lukáš Grajciar, Jiří Čejka, Arnošt Zúkal, Carlos Otero Areán, Gemma Turnes Palomino, and Petr Nachtigall. Controlling the adsorption enthalpy of CO_2 in zeolites by framework topology and composition. *ChemSusChem*, 5(10):2011–2022, 2012.
- [3] Nan Jiang, Máté Erdős, Othonas A. Moulto, Ran Shang, Thijs J.H. Vlught, Sebastiaan G.J. Heijman, and Luuk C. Rietveld. The adsorption mechanisms of organic micropollutants on

- high-silica zeolites causing s-shaped adsorption isotherms: An experimental and monte carlo simulation study. *Chemical Engineering Journal*, 389:123968, 2020.
- [4] Mario Santoro, Federico Gorelli, Julien Haines, Olivier Cambon, Claire Levelut, and Gaston Garbarino. Silicon carbonate phase formed from carbon dioxide and silica under pressure. *Proceedings of the National Academy of Sciences*, 108(19):7689–7692, 2011.
- [5] Johanna Lill, Catherine Dejoie, Carlotta Giacobbe, and Andrew N. Fitch. Adsorption of CO₂ molecules in silicalite: Structural investigation and isotherm modeling using in situ high-resolution powder x-ray diffraction. *The Journal of Physical Chemistry C*, 126(4):2214–2225, 2022.
- [6] Esmail R. Monazam, Lawrence J. Shadle, David C. Miller, Henry W. Pennline, Daniel J. Fauth, James S. Hoffman, and McMahan L. Gray. Equilibrium and kinetics analysis of carbon dioxide capture using immobilized amine on a mesoporous silica. *AIChE Journal*, 59(3):923–935, 2013.
- [7] Esmail R. Monazam, James Spenik, and Lawrence J. Shadle. Fluid bed adsorption of carbon dioxide on immobilized polyethylenimine (PEI): Kinetic analysis and breakthrough behavior. *Chemical Engineering Journal*, 223:795–805, 2013.
- [8] Lucy C. Auton, Maria Aguares, Abel Valverde, Timothy G. Myers, and Marc Calvo-Schwarzwalder. Analytical investigation into solute transport and sorption via intra-particle diffusion in the dual-porosity limit, 2024. submitted to Applied Mathematical Modelling.
- [9] Peter Atkins and Julio de Paula. *Physical Chemistry*. W.H. Freeman & Company, 8 edition, mar 2006.